

## Probing astrophysically important states in the $^{26}\text{Mg}$ nucleus to study neutron sources for the $s$ process

R. Talwar,<sup>1,\*</sup> T. Adachi,<sup>2</sup> G. P. A. Berg,<sup>1</sup> L. Bin,<sup>3</sup> S. Bisterzo,<sup>4,5</sup> M. Couder,<sup>1</sup> R. J. deBoer,<sup>1</sup> X. Fang,<sup>1</sup> H. Fujita,<sup>2,3</sup> Y. Fujita,<sup>2,3</sup> J. Görres,<sup>1</sup> K. Hatanaka,<sup>2</sup> T. Itoh,<sup>3</sup> T. Kadoya,<sup>6</sup> A. Long,<sup>1</sup> K. Miki,<sup>2</sup> D. Patel,<sup>1</sup> M. Pignatari,<sup>7,8,†</sup> Y. Shimbara,<sup>9</sup> A. Tamii,<sup>2</sup> M. Wiescher,<sup>1</sup> T. Yamamoto,<sup>2</sup> and M. Yosoi<sup>2</sup>

<sup>1</sup>*Department of Physics, University of Notre Dame, Notre Dame, Indiana 46556, USA*

<sup>2</sup>*Research Center for Nuclear Physics, Osaka University, Ibaraki, Osaka 567-0047, Japan*

<sup>3</sup>*Department of Physics, Osaka University, Toyonaka, Osaka 560-0043, Japan*

<sup>4</sup>*Department of Physics, University of Turin, I-10125 Torino, Italy*

<sup>5</sup>*INAF - Astrophysical Observatory of Turin, I-10025 Pino Torinese, Italy*

<sup>6</sup>*Department of Physics, Kyoto University, Sakyo-ku, Kyoto 606-8501, Japan*

<sup>7</sup>*E. A. Milne Center for Astrophysics, Department of Physics and Mathematics, University of Hull, Hull HU6 7RX, United Kingdom*

<sup>8</sup>*Konkoly Observatory, Research Center for Astronomy and Earth Sciences, Hungarian Academy of Sciences, H-1121 Budapest, Hungary*

<sup>9</sup>*CYRIC, Tohoku University, Aramaki, Aoba, Sendai 980-8578, Japan*

(Received 17 August 2015; revised manuscript received 14 March 2016; published 10 May 2016)

**Background:** The  $^{22}\text{Ne}(\alpha, n)^{25}\text{Mg}$  reaction is the dominant neutron source for the slow neutron capture process ( $s$  process) in massive stars, and contributes, together with  $^{13}\text{C}(\alpha, n)^{16}\text{O}$ , to the production of neutrons for the  $s$  process in asymptotic giant branch (AGB) stars. However, the reaction is endothermic and competes directly with  $^{22}\text{Ne}(\alpha, \gamma)^{26}\text{Mg}$  radiative capture. The uncertainties for both reactions are large owing to the uncertainty in the level structure of  $^{26}\text{Mg}$  near the  $\alpha$  and neutron separation energies. These uncertainties affect the  $s$ -process nucleosynthesis calculations in theoretical stellar models.

**Purpose:** Indirect studies in the past have been successful in determining the energies and the  $\gamma$ -ray and neutron widths of the  $^{26}\text{Mg}$  states in the energy region of interest. But, the high Coulomb barrier hinders a direct measurement of the resonance strengths, which are determined by the  $\alpha$  widths for these states. The goal of the present experiments is to identify the critical resonance states and to precisely measure the  $\alpha$  widths by  $\alpha$ -transfer techniques.

**Methods:** The  $\alpha$ -inelastic scattering and  $\alpha$ -transfer measurements were performed on a solid  $^{26}\text{Mg}$  target and a  $^{22}\text{Ne}$  gas target, respectively, using the Grand Raiden Spectrometer at the Research Center for Nuclear Physics in Osaka, Japan. The  $(\alpha, \alpha')$  measurements were performed at  $0.45^\circ$ ,  $4.1^\circ$ ,  $8.6^\circ$ , and  $11.1^\circ$  and the  $(^6\text{Li}, d)$  measurements at  $0^\circ$  and  $10^\circ$ . The scattered  $\alpha$  particles and deuterons were detected by the focal plane detection system consisting of multiwire drift chambers and plastic scintillators. The focal plane energy calibration allowed the study of  $^{26}\text{Mg}$  levels from  $E_x = 7.69$ – $12.06$  MeV in the  $(\alpha, \alpha')$  measurement and  $E_x = 7.36$ – $11.32$  MeV in the  $(^6\text{Li}, d)$  measurement.

**Results:** Six levels ( $E_x = 10717$ ,  $10822$ ,  $10951$ ,  $11085$ ,  $11167$ , and  $11317$  keV) were observed above the  $\alpha$  threshold in the region of interest ( $10.61$ – $11.32$  MeV). The  $\alpha$  widths were calculated for these states from the experimental data. The results were used to determine the  $\alpha$ -capture induced reaction rates.

**Conclusion:** The energy range above the  $\alpha$  threshold in  $^{26}\text{Mg}$  was investigated using a high resolution spectrometer. A number of states were observed for the first time in  $\alpha$ -scattering and  $\alpha$ -transfer reactions. The excitation energies and spin-parities were determined. Good agreement is observed for previously known levels in  $^{26}\text{Mg}$ . From the observed resonance levels the  $E_x = 10717$  keV state has a negligible contribution to the  $\alpha$ -induced reaction rates. The rates are dominated in both reaction channels by the resonance contributions of the states at  $E_x = 10951$ ,  $11167$ , and  $11317$  keV. The  $E_x = 11167$  keV state has the most appreciable impact on the  $(\alpha, \gamma)$  rate and therefore plays an important role in the prediction of the neutron production in  $s$ -process environments.

DOI: [10.1103/PhysRevC.93.055803](https://doi.org/10.1103/PhysRevC.93.055803)

### I. INTRODUCTION

The  $^{22}\text{Ne}(\alpha, n)^{25}\text{Mg}$  reaction is one of the dominant neutron sources for the  $s$  process in stars [1]. The reaction occurs in

He-burning environments in massive stars ( $M > 8M_\odot$ ) and in low- and intermediate-mass stars during the asymptotic giant branch phase. During He burning, the bulk of  $^{22}\text{Ne}$  is made by the reaction sequence  $^{14}\text{N}(\alpha, \gamma)^{18}\text{F}(\beta^+, \nu)^{18}\text{O}(\alpha, \gamma)^{22}\text{Ne}$ . This sequence is initiated on the high abundance of the nucleus  $^{14}\text{N}$  in the ashes of the CNO cycle during the preceding hydrogen burning phase of main sequence stars [2,3].

\*rtalwar@anl.gov

†Also with the NuGrid Collaboration, <http://www.nugridstars.org>

The understanding of  $s$ -process nucleosynthesis is of considerable importance. The  $s$  process is responsible for the formation of about half of the elements heavier than iron [4]. It proceeds along the line of stability via a sequence of neutron capture reactions on stellar seed material followed by the  $\beta$  decay of short-lived reaction products.

It determines, together with the rapid neutron capture process ( $r$  process) [5], the distribution of most of the elements heavier than Fe in the solar system. The dominant astrophysical source of the  $r$  process is still a matter of debate [6–8], and the large nuclear physics uncertainties affecting the  $r$ -process path limit the predictive power of theoretical  $r$ -process predictions.

The residual method is a critical tool for extracting the  $r$ -process pattern in the solar system, which is given by the solar abundances after removing the  $s$ -process contribution [9,10]. In general, the  $r$ -process residual identified in the solar system has been shown to be compatible with the  $r$ -process abundance pattern observed in very old metal-poor stars [4], keeping into account a number of relevant differences [11–13]. A detailed understanding of the  $s$ -process abundance distribution is therefore critical for a reliable identification of all possible contributions responsible for these deviations.

At low metallicity, the elemental products of the  $s$ -process nucleosynthesis in asymptotic giant branch (AGB) stars can be directly observed in carbon-enhanced metal-poor stars [4,14–16], in post-AGB stars [17,18], and in Ba stars [19]. For several cases the observations seem to agree well with theoretical model predictions [20,21], while for other cases there are problems reproducing the observations [18,22]. At low metallicity it might be possible to observe the  $s$ -process activated in fast rotating massive stars [23–25]. At metallicities much closer to solar, the chemical composition of planetary nebulae is affected by  $s$ -process nucleosynthesis in the central AGB star [26], which represents the exposed core of the original star forming the planetary nebula. Of great importance is the observation and measurement of isotopic abundances of  $s$ -process products that can be directly derived from the analysis of meteoritic inclusions [27].

The  $s$ -process distribution in the solar system has been divided into three components. Between Fe and Sr there is the weak  $s$ -process component, associated with the  $s$ -process production in massive stars [2,28,29]. Between the Sr neutron-magic peak and Pb there is the main  $s$ -process component [3]. Since the main neutron seed for the build-up of the  $s$ -elements,  $^{56}\text{Fe}$ , scales with stellar metallicity, for stars with sufficiently small metallicity, the neutrons released by the primary source  $^{13}\text{C}$  overcome the first and second  $s$  peaks and directly feed  $^{208}\text{Pb}$ , which is the termination point of the  $s$  process. This characterizes the strong  $s$ -process component [3] which leads to the production of half of the solar  $^{208}\text{Pb}$ .

In low mass ( $1.5 - 3M_{\odot}$ ) AGB stars,  $^{13}\text{C}(\alpha,n)^{16}\text{O}$  is the main neutron source during the interpulse period, while  $^{22}\text{Ne}(\alpha,n)^{25}\text{Mg}$  is marginally activated during advanced thermal pulses ( $T \approx 0.3$  GK) [3]. In case of AGB stars with intermediate initial mass ( $M > 3M_{\odot}$ ), much higher temperatures are readily achieved ( $T \approx 0.35$  GK) thereby efficiently activating the  $^{22}\text{Ne}(\alpha,n)^{25}\text{Mg}$  reaction [21,30]. The  $^{13}\text{C}(\alpha,n)^{16}\text{O}$  reaction plays a marginal role in this AGB mass range [30].

The dominant site for the weak  $s$ -process component is the core-helium burning in massive stars. The neutron flux is expected to be much lower than in AGB stars; therefore, only  $s$ -process isotopes with  $A < 90$  are generated during this phase. The  $^{22}\text{Ne}(\alpha,n)^{25}\text{Mg}$  reaction is considered the most important neutron source [28]. However, due to the negative  $Q$  value ( $Q = -0.478$  MeV) of the reaction, higher temperatures are required to warrant a sufficiently high neutron flux. Therefore the main neutron production is expected toward the final phase of core helium burning when the helium fuel has substantially declined and the core has started to contract under its own gravitational weight. This contraction increases the temperature and density conditions and turns the  $^{22}\text{Ne}(\alpha,n)^{25}\text{Mg}$  reaction into a viable neutron source.

Because of the rapid decline in helium fuel, not all  $^{22}\text{Ne}$  might be consumed [31]. Therefore the  $\alpha$  particles generated via the  $^{12}\text{C}(^{12}\text{C},\alpha)^{20}\text{Ne}$  reaction channel during the subsequent C-burning phase will reactivate the  $^{22}\text{Ne}(\alpha,n)^{25}\text{Mg}$  reaction [32]. Along with  $\alpha$  particles, protons also become readily available at the same time via the  $^{12}\text{C}(^{12}\text{C},p)^{23}\text{Na}$  reaction. Hence, in this scenario, the  $^{22}\text{Ne}(p,\gamma)^{23}\text{Na}$  reaction becomes the main competitor of the  $^{22}\text{Ne}$  neutron source [29]. Nonetheless, the  $s$ -process nucleosynthesis occurs during convective shell C-burning at a high neutron density and with neutron exposure comparable to that in the previous He-core burning stage [2,29].

A recent paper by Liu *et al.* [33] analyzed the strength of the  $^{22}\text{Ne}(\alpha,n)^{25}\text{Mg}$  neutron source on the basis of the observed barium isotopic abundance distribution in meteoritic inclusions. They found that the reaction rate is most likely smaller than that predicted in the NACRE reaction rate tabulation [34], which was based on an earlier analysis of the reaction rate [35]. This conclusion is based on the lower neutron flux conditions required to match the observed barium isotope abundances. This is an interesting assessment but it does not take into account the more complex issue of the interplay between the  $^{22}\text{Ne}(\alpha,n)^{25}\text{Mg}$  and the  $^{22}\text{Ne}(\alpha,\gamma)^{26}\text{Mg}$  reactions influencing the  $^{22}\text{Ne}$  abundance.

As already pointed out in earlier work [35], an important aspect in the discussion of the  $^{22}\text{Ne}(\alpha,n)^{25}\text{Mg}$  reaction as an effective neutron source is the competing  $^{22}\text{Ne}(\alpha,\gamma)^{26}\text{Mg}$  radiative capture process. Radiative capture reactions are facilitated through the electro-magnetic forces and are therefore typically weaker than nuclear reactions with cross sections based on the strong force. However, the  $^{22}\text{Ne}(\alpha,\gamma)^{26}\text{Mg}$  reaction has a positive  $Q$  value and therefore is effective during the entire helium burning phase, where it can substantially reduce the amount of  $^{22}\text{Ne}$  before the  $^{22}\text{Ne}(\alpha,n)^{25}\text{Mg}$  reaction—with its negative  $Q$  value—will start operating. This may not affect the neutron production during the rapidly occurring helium flashes in TP-AGB stars, but it may significantly affect the weak  $s$ -process nucleosynthesis that operates on much longer timescales. If the  $^{22}\text{Ne}(\alpha,\gamma)^{26}\text{Mg}$  reaction is sufficiently strong, the limited  $^{22}\text{Ne}$  abundance may be too low for efficient neutron production in the late phase of helium burning and may reduce neutron production during carbon burning. The overall neutron yield is therefore not only governed by the abundance of  $^{22}\text{Ne}$  but also by the branching ratio between the  $\gamma$  and  $n$  exit channels. For both channels the reaction rates are influenced

by the resonance levels in the  $^{26}\text{Mg}$  compound nucleus. A strong  $^{22}\text{Ne}(\alpha, \gamma)^{26}\text{Mg}$  reaction would reduce the overall  $^{22}\text{Ne}$  abundance during low temperature He burning and reduce the neutron flux at higher temperature conditions. Therefore a complete understanding of both reactions is necessary to understand this interplay between these two reaction channels. The goal of this paper is to deliver a comprehensive study of these levels above the  $\alpha$  threshold in  $^{26}\text{Mg}$  and to explore the impact on the respective reaction rates.

From here onward, all the energy values are given in the center-of-mass frame unless mentioned otherwise.

## II. ALPHA CLUSTER STRUCTURE IN HELIUM BURNING

It is well known that for nuclear reactions associated with light nuclei the nuclear structures of the compound and final nuclei may substantially influence the various resonant and nonresonant contributions to the reaction cross section. This is in particular critical for near threshold contributions that directly influence the stellar reaction rates [36]. Reactions in stellar hydrogen burning primarily proceed through direct capture and resonances associated with pronounced single-particle structures in the compound nuclei. This characterizes the reaction rates in the  $pp$  chains and the CNO cycles in main sequence stars. Reactions in stellar helium burning on the other hand are characterized by the contributions of resonances that can be identified as  $\alpha$ -cluster configurations in the respective compound nuclei. Such  $\alpha$ -cluster configurations are expected in even-even nuclei near the threshold for breakup into an  $\alpha$  particle plus the residual core nucleus as expressed by the ‘‘Ikeda rule’’ [37]. An  $\alpha$  particle represents a cluster of two protons and two neutrons. Such a closed shell configuration makes  $\alpha$  particle particularly stable in self-conjugate nuclei owing to pairing effects. There are a number of theoretical model approaches to calculate cluster configurations in light and medium mass nuclei [38] that were recently complemented by shell model techniques to calculate  $\alpha$  clustering and spectroscopic factors in  $sd$ -shell nuclei [39]. Such cluster configurations are preferably populated in  $\alpha$ -capture and  $\alpha$ -transfer reactions but should also reflect in inelastic  $\alpha$  scattering [40–43].

The most famous example for the impact of  $\alpha$ -cluster structure is the ground state of  $^8\text{Be}$  and the Hoyle state, a pronounced three  $\alpha$ -cluster configuration in  $^{12}\text{C}$  that corresponds to a  $0^+$  resonance level at 7.65 MeV. Both of these levels facilitate the triple- $\alpha$  process leading to the formation of  $^{12}\text{C}$  in stars [44]. Other pronounced  $\alpha$ -cluster resonance configurations have been found in  $^{16}\text{O}$ , influencing the  $^{12}\text{C}(\alpha, \gamma)^{16}\text{O}$  reaction [45], and in  $^{22}\text{Ne}$ , responsible for the fast conversion of  $^{18}\text{O}$  via the  $^{18}\text{O}(\alpha, \gamma)^{22}\text{Ne}$  radiative capture reaction to  $^{22}\text{Ne}$  [46].

There are a number of similar cases of low energy resonances with pronounced  $\alpha$ -cluster structure and, indeed, like in  $^{22}\text{Ne}$ , other  $T = 1$  ( $N \neq Z$ ) nuclei such as  $^{18}\text{O}$  [47] and  $^{26}\text{Mg}$  [48] exhibit resonance features that correspond to  $\alpha$ -cluster states. The identification of  $\alpha$  clusters should be based on small single-particle and large  $\alpha$ -spectroscopic factors. Such levels are characterized by large resonance strength in  $\alpha$ -capture and transfer reactions, but should only

be weakly populated by single-particle capture and transfer process. However, in low energy radiative capture to resonance states near the  $\alpha$  threshold, the strength is suppressed by the Coulomb barrier, while  $\alpha$ -transfer reactions to these very states reflect the full  $\alpha$ -strength distribution.

Considerable efforts have been made in the past to perform direct measurements of the  $^{22}\text{Ne}(\alpha, n)^{25}\text{Mg}$  [49–54] and the  $^{22}\text{Ne}(\alpha, \gamma)^{26}\text{Mg}$  [53,55] reactions. In the astrophysical region of interest,  $\alpha$  penetrability is largely suppressed by the Coulomb barrier. The reaction cross-section is therefore very difficult to measure because of the cosmic and beam-induced background. Only upper limits have been obtained for the  $n$  and  $\gamma$  yields at energies below the lowest directly observed resonance at  $E_R = 702$  keV ( $E_x = 11.317$  MeV).

A number of scattering and transfer measurements [48,56–61] have been performed to investigate the level structure of  $^{26}\text{Mg}$  above the  $\alpha$  threshold (10614.75(3) keV [62]) as well as above the  $n$  threshold (11093.09(4) keV [62]). The  $^{26}\text{Mg}(\alpha, \alpha')^{26}\text{Mg}$  measurement by Borg *et al.* [58] exhibited poor resolution ( $\sim 120$  keV) and the  $^{22}\text{Ne}({}^6\text{Li}, d)^{26}\text{Mg}$  measurements by Giesen *et al.* [48] and Ugalde *et al.* [59] were handicapped by high beam-induced background resulting in huge contamination peaks in the astrophysical region of interest. These measurements were complemented by the study of additional reaction channels such as  $^{25}\text{Mg}(n, \gamma)^{26}\text{Mg}$  [60,63], inelastic proton scattering measurements on  $^{26}\text{Mg}$  [64] using the Grand Raiden Spectrometer at RCNP, Osaka, Japan, as well as studies of  $^{26}\text{Mg}(\gamma, \gamma')^{26}\text{Mg}$  by Longland *et al.* [61] and deBoer *et al.* [65] and by  $^{26}\text{Mg}(\gamma, n)^{25}\text{Mg}$  measurement by deBoer *et al.* [66]. The results did provide additional information on the  $n$  and  $\gamma$  widths of the near threshold levels and added important spin-parity information about the  $\alpha$ -unbound states in  $^{26}\text{Mg}$ . However, the critical parameter that needs to be determined for deriving the  $^{22}\text{Ne} + \alpha$  resonance strengths is the  $\alpha$  partial width of these states.

In the present work,  $\alpha$ -inelastic scattering (with improved resolution of  $\simeq 65$  keV with respect to the 120 keV resolution obtained by Borg *et al.* [58]) and  $\alpha$  transfer via  $({}^6\text{Li}, d)$  (with a well-defined background shape using thick target yield function [67]) have been used to probe the  $^{26}\text{Mg}$  nucleus using the Grand Raiden Spectrometer. The main goal is to determine the resonance energies and  $\alpha$  widths for levels above the  $\alpha$  threshold, serving as input parameters into the  $^{22}\text{Ne} + \alpha$  capture reaction rate calculation. The  $\alpha$  widths will also help establish the predicted  $\alpha$ -cluster structure for these levels.

## III. EXPERIMENTAL SETUP

To study the low energy resonances in  $^{22}\text{Ne} + \alpha$ ,  $^{26}\text{Mg}(\alpha, \alpha')^{26}\text{Mg}$  and  $^{22}\text{Ne}({}^6\text{Li}, d)^{26}\text{Mg}$  reactions have been measured using the high resolution Grand Raiden (GR) Spectrometer at the Research Center for Nuclear Physics (RCNP) in Osaka, Japan. Both experiments were designed to cover the energy range of interest ( $E_x = 10.61$ – $11.32$  MeV) in the  $^{26}\text{Mg}$  nucleus.

For the  $\alpha$ -inelastic scattering measurement, a self-supporting  $^{26}\text{Mg}$  target (enriched to 99.4%) of thickness  $1.16$  mg/cm $^2$  was used. Since  $^{26}\text{Mg}$  oxidizes rapidly when

exposed to air, impurity peaks corresponding to  $^{16}\text{O}$  were observed in addition to those owing to carbon contamination. Background runs were taken on  $\text{CH}_2$  ( $1.13 \text{ mg/cm}^2$ ) and Mylar [ $(\text{C}_{10}\text{H}_8\text{O}_4)_n$ ] ( $1 \text{ mg/cm}^2$ ) targets. For focal plane energy calibration, the  $^{25}\text{Mg}(\alpha, ^3\text{He})^{26}\text{Mg}$  reaction was measured, which populated a significant part of the focal plane with well-known low energy levels in  $^{26}\text{Mg}$  [68].

A 206 MeV  $\alpha$  beam was generated using the coupled Azimuthally Varying Field (AVF) and Ring cyclotrons and was transported via the fully dispersion matched West South (WS) beam line [69] to the target chamber upstream of the GR spectrometer. The new WS beam line has been designed to satisfy all the required matching conditions [70]: focusing condition, lateral dispersion matching, kinematic correction, and angular dispersion matching. For the present measurements, the faint-beam method was applied wherein a low intensity beam ( $10^3$  particles/s) was directly sent into the spectrometer, placed at  $0^\circ$ , so that the matching conditions could be diagnosed using the beam properties in the focal plane [71]. This technique ensured that the final resolution was not limited by the momentum spread (150–200 keV) of the beam exiting from the cyclotron.

The scattered  $\alpha$  particles emerging from the target were momentum analyzed by the GR spectrometer (Fig. 1) with a high resolving power of  $p/\Delta p = 37000$  [72]. They were detected at the focal plane detection system, which consisted of two multiwire drift chambers (MWDCs) and a stack of 3 and 10 mm thick plastic scintillators (PS1 and PS2) along with a 2 mm thick aluminum absorber placed between the two scintillators. The MWDCs provided position and angular information in the horizontal and vertical directions and the scintillators gave time-of-flight and energy loss information for particle identification. In order to precisely reconstruct the vertical component of the scattering angle at and near  $0^\circ$ , the off-focus mode [73] was employed. A sieve slit

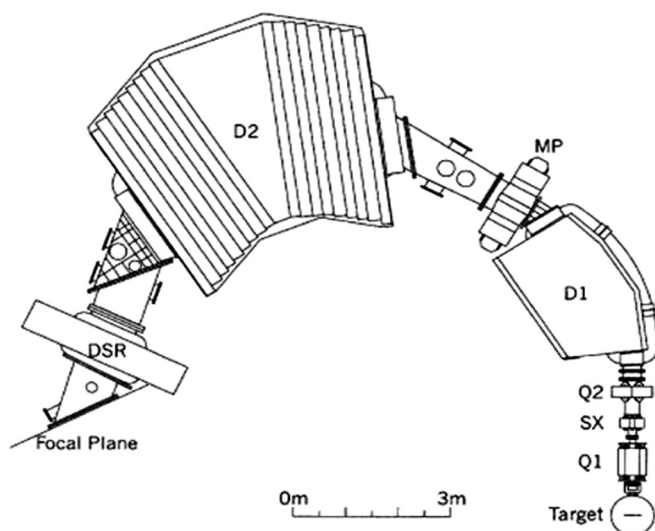


FIG. 1. Schematic layout of the Grand Raiden Spectrometer at RCNP. The dipole magnet for spin rotation (DSR) was not used in the present experiments, but it is a part of the permanent installation. Figure from Ref. [69].

(multihole aperture) was used to perform the angle calibration measurement. A special beam exit pipe was incorporated in the exit window of the focal plane to collect the beam at  $0.45^\circ$  in the Faraday cup downstream of the focal plane detector. The Faraday cup downstream of quadrupole Q1 was used for  $2^\circ$ – $6^\circ$  settings of the spectrometer, and for higher angles the cup inside the scattering chamber was used.

For the  $\alpha$ -transfer measurement, highly enriched  $^{22}\text{Ne}$  gas (enrichment  $>99\%$ ) was pressurized to 0.2 atm in a gas cell using a gas handling system [74]. The cell body was machined from copper and the gas was filled into a volume measuring 44 mm by 14 mm by 10 mm. Aramid ( $\text{C}_{14}\text{O}_2\text{N}_2\text{Cl}_2\text{H}_8$ ) films of thickness  $4 \mu\text{m}$  were used as entrance and exit windows to cover the aperture in the cell body. In addition to the  $^{22}\text{Ne}$  gas target, ( $^6\text{Li}, d$ ) measurements were also performed on the  $4 \mu\text{m}$  Aramid foil, and the  $^{16}\text{O}$  and  $^{20}\text{Ne}$  gas targets to identify background peaks and perform focal plane energy calibration using the well-known low energy peaks [75,76].

A  $^6\text{Li}$  beam with an energy of  $E_{\text{lab}} = 82.3 \text{ MeV}$  was generated using the AVF cyclotron. All other experimental procedures and setups were the same as those for the  $\alpha$ -inelastic scattering measurement. Exceptions were (a) the use of a stack of two plastic scintillators each of thickness 10 mm and (b) the  $0^\circ$  Faraday cup was placed inside the first dipole D1 because the  $B\rho$  ratio of deuteron to  $^6\text{Li}$  is 1.7.

#### IV. DATA ANALYSIS AND RESULTS

The 5% momentum acceptance of the Grand Raiden Spectrometer allowed an excitation energy range coverage of 3–12 MeV in the  $(\alpha, \alpha')$  experiment and 7–12 MeV in the  $(^6\text{Li}, d)$  experiment, for a single magnetic field setting.

Appropriate gates were set on the scattered  $\alpha$  particles and deuterons in the time-of-flight as well as the energy loss spectra coming from the plastic scintillators. This reduced the background coming from multiple scattering events. The first-order dependence of the resolution on the energy spread of the incident beam was eliminated using the dispersion matching technique [71]. However, the effects of reaction kinematics and higher-order magnetic aberrations had to be corrected for during the offline analysis. This resulted in a resolution of 65 keV for the  $(\alpha, \alpha')$  measurement and 100 keV for the  $(^6\text{Li}, d)$  measurement. These values include the effects of energy losses through the solid  $^{26}\text{Mg}$  target (22 keV), the  $^{22}\text{Ne}$  gas target (11 keV), and energy straggling in the entrance and exit foils of the gas cell, along with the effects of angular straggling of the beam through these foils.

##### A. Energy calibration and peak identification

Establishing a well-defined relationship between the magnetic rigidity ( $B\rho$ ) of the outgoing particle and its corresponding position at the focal plane was an important prerequisite to accurately determine the excitation energies associated with the inelastic scattering and  $\alpha$ -transfer peaks. Precise determination of the focal plane position was achieved using an asymmetric Gaussian function plus polynomial background to fit the  $(\alpha, \alpha')$  peaks and a Gaussian function plus arctangent background [67] to fit the  $(^6\text{Li}, d)$  peaks and the thick target Aramid background (Fig. 3). Magnetic rigidities were

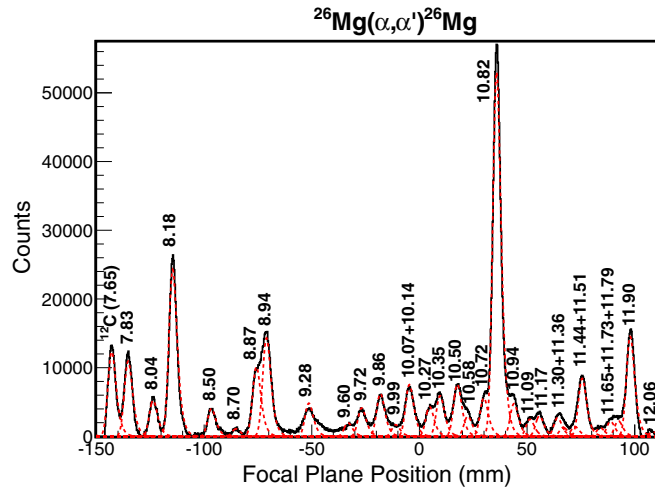


FIG. 2. Background-subtracted spectrum showing  $^{26}\text{Mg}$  peaks coming from the  $(\alpha, \alpha')$  measurement at a spectrometer angle of  $0.45^\circ$ . All energies are in MeV. The red dashed lines represent the individual peaks.

determined for the well-known low-lying states populated in  $^{26}\text{Mg}$  [77] via the  $^{25}\text{Mg}(\alpha, ^3\text{He})$  reaction [68], in  $^{20}\text{Ne}$  [78] via the  $^{16}\text{O}({}^6\text{Li}, d)$  reaction [75], and in  $^{24}\text{Mg}$  [79] via the  $^{20}\text{Ne}({}^6\text{Li}, d)$  reaction [76]. Using these peaks, mainly linear calibration functions with small quadratic terms were established that allowed identification of  $^{26}\text{Mg}$  peaks with ranges  $E_x = 7.69$ – $12.06$  MeV at  $0.45^\circ$ ,  $4.1^\circ$ ,  $8.6^\circ$ , and  $11.1^\circ$  in the  $(\alpha, \alpha')$  measurement (Fig. 2) and  $E_x = 7.36$ – $11.32$  MeV at  $0^\circ$  and  $10^\circ$  in the  $({}^6\text{Li}, d)$  measurement (Fig. 4). The results for the excitation energies were determined by taking a weighted average of the energies measured at different angles. The errors associated with these energies were computed as a quadratic combination of the statistical error [3–8 keV for  $(\alpha, \alpha')$  measurement and 12–30 keV for  $({}^6\text{Li}, d)$  measurement] arising from uncertainties in energy loss calculations using SRIM [80] and the number of counts in the peak, and the systematic error

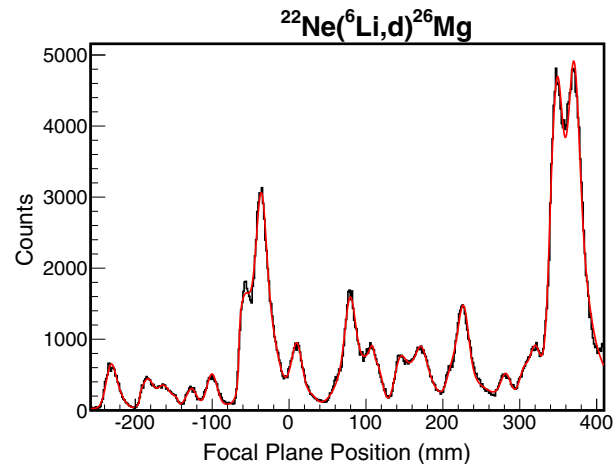
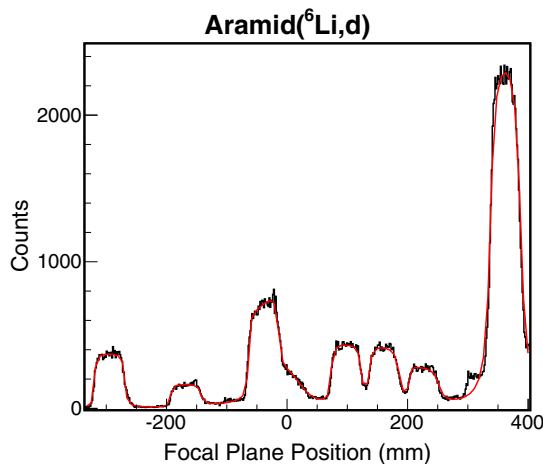


FIG. 3. Left: Background spectrum arising from Aramid  $({}^6\text{Li}, d)$  measurement. The red solid line represents the total fit comprising the arctangent function used to describe the background. Right:  $^{26}\text{Mg}$  peaks coming from the  $0^\circ$   $({}^6\text{Li}, d)$  measurement. The red solid line represents the total fit comprising the Gaussian function for the  $^{26}\text{Mg}$  peaks plus the arctangent function for the Aramid background

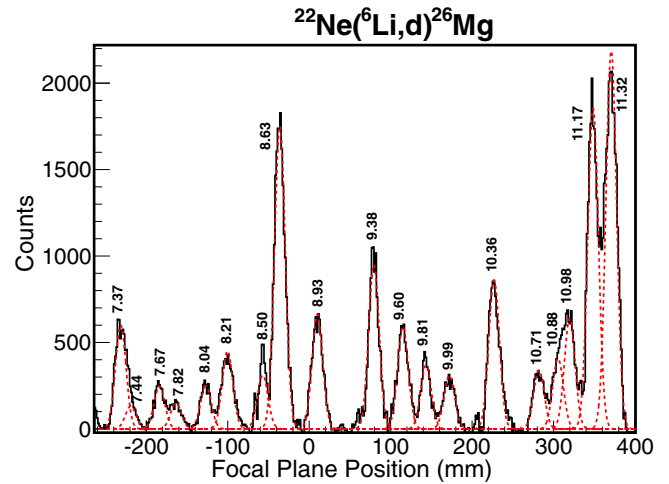


FIG. 4. Background subtracted spectrum showing  $^{26}\text{Mg}$  peaks coming from the  $0^\circ$   $({}^6\text{Li}, d)$  measurement. All energies are in MeV. The red dashed lines represent the individual peaks.

(5–10 keV for both measurements) arising from uncertainties in energy calibration, target inhomogeneities, and reaction angle determinations.

The observed excitation energies are presented in four tables: (i) energy levels measured in the present work along with the adopted values in Table I; (ii) energy levels below the  $\alpha$  threshold (10614.75(3) keV [62]) in Table II; (iii) energy levels above the  $\alpha$  threshold (10614.75(3) keV [62]) and below the neutron threshold (11093.09(4) keV [62]) in Table III; and (iv) energy levels above the neutron threshold (11093.09(4) keV [62]) in Table IV. In the last three tables, the observed levels were compared with previous results.

## B. Angular distribution analysis

The angular distributions in the present work were studied using the general purpose inelastic coupled channel code called PTOLEMY [81] for  $(\alpha, \alpha')$  and the state-of-the-art code

TABLE I. The  $^{26}\text{Mg}$  excitation energies measured in the present work along with the adopted values. The numbers in parenthesis are the uncertainties in the last digits of the energy values.

Present work		Adopted value
$^{26}\text{Mg}(\alpha, \alpha')^{26}\text{Mg}$ $E_x$ (keV)	$^{22}\text{Ne}(^6\text{Li}, d)^{26}\text{Mg}$ $E_x$ (keV)	$E_x$ (keV)
	7365(13)	7365(13)
7688(7)	7671(16)	7685(8)
7827(6)	7821(22)	7826(6)
8035(7)	8040(13)	8036(7)
8185(9)	8214(14)	8193(15)
8497(8)		8497(8)
8626(7)	8625(15)	8626(7)
8703(6)		8703(6)
8866(9)		8866(9)
8938(6)	8931(13)	8937(6)
9276(10)		9276(10)
	9383(16)	9383(16)
9604(9)	9595(32)	9603(9)
9718(7)		9718(7)
9863(6)		9863(6)
9993(9)	9987(18)	9992(8)
10067(7)		10067(7)
10136(8)		10136(8)
10273(10)		10273(10)
10350(7)	10357(14)	10351(7)
10495(9)		10495(9)
10575(10)		10575(10)
10718(10)	10714(20)	10717(9)
10822(10)		10822(10)
10937(11)	10977(15)	10951(21)
11085(8)		11085(8)
11167(9)	11169(17)	11167(8)
11301(9)		11301(9)
	11317(18)	11317(18)
11359(8)		11359(8)
11445(9)		11445(9)
11509(11)		11509(11)
11648(7)		11648(7)
11731(9)		11731(9)
11824(9)		11824(9)
11900(9)		11900(9)
12064(8)		12064(8)

for transfer reactions called FRESKO [82] for  $(^6\text{Li}, d)$ , under the assumption that the observed peaks are the result of a single level in  $^{26}\text{Mg}$ . The starting set of optical potential parameters were adopted from references [58,83,84] and were then modified to best fit the present  $^{26}\text{Mg}(\alpha, \alpha')^{26}\text{Mg}$  and  $^{22}\text{Ne}(^6\text{Li}, d)^{26}\text{Mg}$  data. The final set of optical parameters are given in Tables V and VI. For the  $\alpha$ -transfer study, Woods-Saxon potentials were used to define the different reaction channels. The number of radial nodes  $N$  and the orbital momentum  $L$  were fixed by the Talmi-Moshinsky relation,  $\sum_{i=1}^4 (2n_i + l_i)$ , where  $n_i, l_i$  refer to the harmonic oscillator quantum numbers of each transferred nucleon [48]. For all positive parity states ( $L = \text{even}$ ), the  $(sd)^4$  configuration

was assumed resulting in  $2N + L = 8$  and for all negative parity states ( $L = \text{odd}$ ), the  $(sd)^3(fp)$  configuration was assumed giving  $2N + L = 9$ . Figures 5, 6, and 7 show the resulting angular distributions for the  $(\alpha, \alpha')$  and the  $(^6\text{Li}, d)$  measurements, respectively. The error bars associated with the experimental data points in these figures correspond to both the statistical error as well as 5% systematic error. Since these figures are using a logarithmic scale, the combined error is in general within the size of the symbol. For all the states observed in the present work, spin assignments are available in the literature. Hence, only angular distributions for the available choice of spins have been shown. No final spin assignments were based merely on the present measurements alone.

### C. Discussion of peaks above the $\alpha$ threshold

Above the  $\alpha$ -threshold (10614.75(3) keV [62]), the following peaks have been observed in the region of interest ( $E_x = 10.61\text{--}11.32$  MeV):  $E_x = 10717(9)$ , 10822(10), 10951(21), 11085(8), 11167(8) and 11317(18) keV. These energies are weighted averages of the energies measured in the present  $(\alpha, \alpha')$  and  $(^6\text{Li}, d)$  experiments. Peaks corresponding to all of these states have been seen in the  $(\alpha, \alpha')$  experiment at all four angles,  $0.45^\circ$ ,  $4.1^\circ$ ,  $8.6^\circ$ , and  $11.1^\circ$ , except for the  $E_x = 11317(18)$  keV state. This state could not be clearly identified because it was partly obscured by the  $E_x = 11301(9)$  keV state and partly by the  $E_x = 11359(8)$  keV state in  $^{26}\text{Mg}$ . In the  $(^6\text{Li}, d)$  experiment, the above mentioned six peaks were observed at  $0^\circ$  and  $10^\circ$  except for the  $E_x = 11167(8)$  keV state and the  $E_x = 11317(18)$  keV state which were observed only at  $0^\circ$ . At  $10^\circ$ , the  $E_x = 11167(8)$  keV peak was partly covered by the  $E_x = 9532.48(10)$  keV state [79] in  $^{24}\text{Mg}$ , and the  $E_x = 11317(18)$  keV peak was partly covered by the  $E_x = 9532.48(10)$  keV state [79] in  $^{24}\text{Mg}$  and partly by the  $E_x = 4247.7(11)$  keV state [78] in  $^{20}\text{Ne}$ . As can be seen in Tables II, III, and IV, the energies in the present work are in good agreement with those from previous transfer measurements with similar energy resolution. For the  $E_x = 10822(10)$  keV state, a comparison has been made with  $E_x = 10805.9(4)$  [77], 10808(20) [59], and 10805.7(7) [61] keV states, instead of the nearby state at  $E_x = 10824(3)$  keV [77], as shown in Table III. The  $E_x = 10824(3)$  keV [77] state was observed by Moss [56] in  $^{26}\text{Mg}(p, p')^{26}\text{Mg}$  measurement and was unambiguously assigned a spin-parity of  $1^+$  by Crawley *et al.* [57]. Since  $\alpha$  particles preferentially populate natural parity states and Longland *et al.* [61] unambiguously assigned a spin-parity of  $1^-$  to the  $E_x = 10805.7(7)$  keV state, the  $E_x = 10822(10)$  keV state observed in the present work has not been compared to the  $E_x = 10824(3)$  keV [77] state. The spin-parity possibilities for these peaks as well as the final adopted values are tabulated in Table VII. Unlike Giesen *et al.* [48], where the high background associated with his data did not allow unique spin assignments, the excited states observed in the present work correspond to lower angular momentum transfer. The  $E_x = 11167(8)$  keV state and the  $E_x = 11317(18)$  keV state require a more detailed discussion.

$E_x = 11317(18)$  keV ( $E_R = 702$  keV,  $J^\pi = 1^-$ ): The angular distribution and the upper limit point shown in Fig. 7 suggest a spin-parity of  $1^-$  for this state, however  $2^+$  distribution cannot

TABLE II. The  $^{26}\text{Mg}$  excitation energies measured below the  $\alpha$ -threshold (10614.75(3) keV [62]) in the present work along with the comparison with previous works. The numbers in parenthesis are the uncertainties in the last digits of the energy values.

Present work adopted value $E_x$ (keV)	Endt98 [77] compilation $E_x$ (keV)	Ugalde <i>et al.</i> [59] $^{22}\text{Ne}(^6\text{Li},d)^{26}\text{Mg}$ $E_x$ (keV)	Present work adopted value $E_x$ (keV)	Endt98 [77] compilation $E_x$ (keV)	Ugalde <i>et al.</i> [59] $^{22}\text{Ne}(^6\text{Li},d)^{26}\text{Mg}$ $E_x$ (keV)	Giesen <i>et al.</i> [48] $^{22}\text{Ne}(^6\text{Li},d)^{26}\text{Mg}$ $E_x$ (keV)
	7200(20)			9371(2)		
	7242(1)		9383(16)	9383(1)		9404(20)
	7261.39(4)			9427.74(7)		
	7282.74(5)			9471(2)		
	7348.87(5)			9541(1)		
7365(13)	7371.2			9560(3)		
	7395(1)			9574.02(6)		
	7428(3)			9579(3)		
	7541.73(5)		9603(9)	9590(2)	9570(40)	9586(20)
	7677(1)			9617.0(9)		
7685(8)	7697.3(6)			9681(2)		
	7725.74(16)		9718(7)	9714(3)		
	7773(1)			9771(2)		
	7816(2)			9779(3)		
7826(6)	7824(3)			9814(2)		
	7840(2)			9829(1)		
	7851(3)		9863(6)	9856.52(6)		
	7953(1)			9883(3)		
8036(7)	8033(2)			9902(2)		
	8052.9(6)			9927(2)		
8193(15)	8184.96(10)			9939(2)		
	8201(1)			9967(2)		
	8227.56(16)			9982(2)		
	8250.70(10)		9992(8)	9989(1)		9985(20)
	8399(3)			10040(2)		
	8458.87(13)		10067(7)	10069(2)		
	8464(2)			10102.41(15)		
	8472(1)			10126.70(10)		
8497(8)	8503.74(9)		10136(8)	10136(3)		
	8532.27(9)			10148(2)		
	8577(3)			10159(3)		
8626(7)	8625(1)			10184(2)		
	8670(1)			10220.1(3)		
8703(6)	8705.73(9)			10234(2)		
8866(9)	8863.8(5)		10273(10)	10271(3)		
	8903.5(6)			10319(2)		
8937(6)	8930(2)			10328(3)		
	8959.4(5)			10341(3)		
	9020(2)		10351(7)	10350.37(12)		10335(20)
	9044.7(3)			10362.42(7)		
	9064(1)			10377(2)		
	9111(1)			10400(15)		
	9169(1)			10414(3)		
	9206(2)			10487(3)		
	9238.7(5)		10495(9)	10493(3)		
	9261(2)			10516(3)		
9276(10)	9281(3)	9320(60)		10529(2)		
	9291(2)			10567(3)		
	9304(2)		10575(10)	10576(2)		10568(25)
	9317(2)			10599.96(7)		
	9325.51(6)					

TABLE III. The  $^{26}\text{Mg}$  excitation energies measured above the  $\alpha$  threshold(10614.75(3) keV [62]) and below the neutron threshold(11093.09(4) keV [62]) in the present work along with the comparison with previous works. The numbers in parenthesis are the uncertainties in the last digits of the energy values.

Present work adopted value $E_x$ (keV)	Endt98 [77] compilation $E_x$ (keV)	Ugalde <i>et al.</i> [59] $^{22}\text{Ne}(^6\text{Li},d)^{26}\text{Mg}$ $E_x$ (keV)	Giesen <i>et al.</i> [48] $^{22}\text{Ne}(^6\text{Li},d)^{26}\text{Mg}$ $E_x$ (keV)	Longland <i>et al.</i> [61] $^{26}\text{Mg}(\gamma,\gamma')^{26}\text{Mg}$ $E_x$ (keV)
	10646(2)			10647.3(8)
	10650(2)			
	10681.9(3)			
	10693(3)			
	10707(3)			
10717(9)	10718.75(9)		10694(20)	
	10726(3)			
	10745.98(12)			
	10767(2)			
10822(10)	10805.9(4)	10808(20)		10805.7(7)
	10824(3)			
	10881(3)			
	10893(3)			
	10915(3)			
	10927(3)			
10951(21)	10945(3)	10953(25)	10949(25)	10949.1(8)
	10978(3)			
	10998(3)			
	11012(3)			
	11048(3)			
11085(8)	11084(3)			

be excluded. Since the resonance strengths for this state are experimentally known, the choice of spin and parity does not have any influence on the reaction rate. However, it influences the scaling factors used to calculate the  $\alpha$  widths for the other states (see Sec. IV D).

Koehler [85] has made an argument that this state cannot correspond to both the  $^{22}\text{Ne}(\alpha,n)^{25}\text{Mg}$  resonance observed at  $E_R^{\text{lab}} = 832(2)$  keV ( $E_x = 11319(2)$  keV) [54] and the  $^{22}\text{Ne}(\alpha,\gamma)^{26}\text{Mg}$  resonance observed at  $E_R^{\text{lab}} = 828(5)$  keV ( $E_x = 11315(5)$  keV) [53]. The basis of his argument is the assumption that, for  $E_R^{\text{lab}} = 832$  keV, the total width  $\Gamma$  is equal to 0.25 (0.17) keV, as reported by Ref. [54]. The energy resolution for the Stuttgart DYNAMITRON accelerator, which was used for the  $^{22}\text{Ne}(\alpha,n)^{25}\text{Mg}$  measurement by Jaeger *et al.* [54], is 1.4 keV [86], independent of the beam energy, and is related to the 120 kHz ripple. Additional contributions arise from the straggling in the gas, the energy reproducibility of 2 keV, and the geometrical solid angle [87]. For these reasons, the quoted width should be interpreted as an upper limit of 0.42 keV and, therefore, the assumption of Koehler is incorrect. In addition, all measurements of these resonance energies [48,51–54] agree well with each other. Furthermore, Jaeger in his thesis [87] fitted his unpublished  $(\alpha,\gamma)$  data with the same parameters he used for the  $(\alpha,n)$  resonance except for the  $\gamma$  and  $n$  widths. This clearly indicates that the resonances observed in the gamma and neutron channels are the same and there is no need to treat them separately, as suggested by Longland *et al.* [88].

The  $(n,\gamma)$  measurements [60,63] have yielded four resonances, at  $E_n = 226.19, 242.45, 244.58,$  and  $245.57$  keV. None of these correspond to the well-known  $E_R^{\text{lab}} = 832 \pm 2$  keV ( $E_n = 235 \pm 2$  keV) resonance, within error bars. Also, the 702 keV ( $E_R^{\text{lab}} = 830$  keV) resonance, observed in the present work, has a pronounced  $\alpha$ -cluster structure, as reflected by its large  $\alpha$ -spectroscopic factor (Table VIII) with a  $\Gamma_\gamma/\Gamma_n$  ratio = 0.3 (determined using  $\omega\gamma_{(\alpha,\gamma)} = 0.036(4)$  meV [53] and  $\omega\gamma_{(\alpha,n)} = 0.118(11)$  meV [54]). This implies that the neutron width associated with this resonance should be small, and, therefore the probability of observing it in an  $(n,\gamma)$  measurement is low.

$E_x = 11167(8)$  keV ( $E_R = 553$  keV,  $J^\pi = 1^-$ ): The cross sections from the  $(\alpha,\alpha')$  experiment follow the  $1^-$  as well as the  $2^+$  angular distributions. But, based on the upper limit derived for this state at  $10^\circ$  in the  $(^6\text{Li},d)$  measurement, the data favor a  $1^-$  angular distribution. However, the possibility of the  $2^+$  distribution shown in Fig. 7 cannot be completely ruled out.

#### D. Reaction rates

The  $\alpha$ -capture rates on  $^{22}\text{Ne}$  have been determined using the narrow resonance reaction rate formalism defined as [34]

$$\begin{aligned}
 N_A \langle \sigma v \rangle &= 1.54 \times 10^5 (\mu T_9)^{-3/2} \\
 &\times \sum_i (\omega\gamma)_i \exp\left(\frac{-11.605 E_{R,i}}{T_9}\right) \\
 &\times (\text{cm}^3 \text{sec}^{-1} \text{mol}^{-1}) \quad (1)
 \end{aligned}$$

TABLE IV. The  $^{26}\text{Mg}$  excitation energies measured above the neutron threshold(11093.09(4) keV [62]) in the present work along with the comparison with previous works. The numbers in parenthesis are the uncertainties in the last digits of the energy values.

Present work adopted value $E_x$ (keV)	Endt98 [77] compilation $E_x$ (keV)	Giesen <i>et al.</i> [48] $^{22}\text{Ne}(^6\text{Li}, d)^{26}\text{Mg}$ $E_x$ (keV)	Massimi <i>et al.</i> [60] $^{25}\text{Mg}(n, \gamma)^{26}\text{Mg}$ $E_x$ (keV)	Jaeger <i>et al.</i> [54] $^{22}\text{Ne}(\alpha, n)^{25}\text{Mg}$ $E_x$ (keV)	Longland <i>et al.</i> [61] $^{26}\text{Mg}(\gamma, \gamma')^{26}\text{Mg}$ $E_x$ (keV)
	11112.2(2)		11112.19(9)		
	11142(6)				
	11153.2(2)		11153.474(43)		11153.5(10)
	11163.3(5)		11163.04(7)		
11167(8)	11169.4(2)		11169.42(7)		
	11171.1(7)		11171.183(41)		
	11183.0(2)		11183.20(6)		
	11188.8(2)		11189.40(6)		
	11191(2)		11191.289(49)		
	11194.5(2)				
			11196.68(6)		
	11243.3(2)		11243.62(6)		
	11274.4(2)		11274.441(49)		
	11279.5(2)		11280.349(49)		
			11285.86(7)		
	11286.6(3)		11286.572(46)		
11301(9)	11289.2(3)		11289.397(41)		
	11294.7(5)		11293.63(5)		
			11296.39(9)		
	11311.0(5)		11310.945(41)		
11317(18)		11310(20)		11319(2)	
	11328.3(5)		11326.56(6)		
	11329(2)		11328.61(7)		
			11329.527(42)		
			11337.31(5)		
11359(8) <sup>a</sup>	11343.7(5)		11345.21(7)		
	11362.0(6)		11362.31(24)		
	11364.9(6)				
	11372.5(6)				
	11392.7(6)		11393.10(5)		
	11425.4(7)				
11445(9) <sup>a</sup>	11439.8(7)	11453(25)	11441.70(6)	11441(2)	
	11457(2)				
	11463.9(8)		11466.29(8)	11461(2)	
	11499.4(8)				
11509(11) <sup>a</sup>	11508.1(9)		11500.82(5)	11506(2)	
	11540.8(9)		11527.60(10)	11526(2)	
	11570(2)				
	11586(1)		11588.88(7)		
	11612(5)		11609.22(6)	11630(2)	
11648(7) <sup>a</sup>	11647(5)	11644(20)			
11731(9) <sup>a</sup>				11749(10)	
	11795(10)			11787(4)	
11824(9) <sup>a</sup>	11828(3)	11831(20)		11828(2)	
	11890(2)				
11900(9) <sup>a</sup>	11910(2)				
	11945(10)				
	11950(2)				
12064(8) <sup>a</sup>	12049(2)				

<sup>a</sup>These peaks were out of the focal plane detection range in the present  $^{22}\text{Ne}(^6\text{Li}, d)^{26}\text{Mg}$  measurement, and hence have not been taken into account in the present work reaction rate calculations.

TABLE V. Optical parameters used in PTOLEMY to study the angular distributions of  $^{26}\text{Mg}(\alpha, \alpha')^{26}\text{Mg}$  cross sections.

Nucleus	$E_\alpha$ (MeV)	V (MeV)	$r_{0R}$ (fm)	$a_R$ (fm)	$V_I$ (MeV)	$r_{0I}$ (fm)	$a_I$ (fm)	$r_{0C}$ (fm)
$^{26}\text{Mg}$	206	100.0	1.20	0.61	25.67	1.50	0.55	1.30

where  $\mu$  is the reduced mass,  $T_0$  is the temperature in GK,  $(\omega\gamma)_i$  is the resonance strength of the  $i$ th resonance in eV, and  $E_{R,i}$  is the resonance energy in the center of mass frame of the  $i$ th resonance in MeV.

The resonance energies were determined using  $E_{R,i} = E_{x,i} - Q$  (10614.75(3) keV [62]) and the resonance strengths were calculated using [34]:

$$\omega\gamma_{(\alpha,\gamma)} = \frac{2J+1}{(2J_1+1)(2J_2+1)} \frac{\Gamma_\alpha \Gamma_\gamma}{\Gamma} \quad (2)$$

and

$$\omega\gamma_{(\alpha,n)} = \frac{2J+1}{(2J_1+1)(2J_2+1)} \frac{\Gamma_\alpha \Gamma_n}{\Gamma}, \quad (3)$$

where  $J$  represents the spin of the resonance and  $J_1$  and  $J_2$  represent the spin of  $^{22}\text{Ne}$  and  $\alpha$  nuclei, respectively, both being equal to 0. Because of the penetrability, for low energy resonances  $\Gamma_\alpha \ll \Gamma_\gamma$  and  $\Gamma_n$  [48,53]. For  $n$ -bound states ( $\Gamma = \Gamma_\alpha + \Gamma_\gamma$ ), Eq. (2) can be written as

$$\omega\gamma_{(\alpha,\gamma)} = (2J+1)\Gamma_\alpha. \quad (4)$$

For  $n$ -unbound states ( $\Gamma = \Gamma_\alpha + \Gamma_\gamma + \Gamma_n$ ), Eqs. (2) and (3) can be written as

$$\omega\gamma_{(\alpha,\gamma)} = (2J+1) \frac{\Gamma_\alpha \Gamma_\gamma}{\Gamma_\gamma + \Gamma_n} \quad (5)$$

and

$$\omega\gamma_{(\alpha,n)} = (2J+1) \frac{\Gamma_\alpha \Gamma_n}{\Gamma_\gamma + \Gamma_n}. \quad (6)$$

With these definitions it follows that for  $\Gamma_\alpha \ll \Gamma_\gamma, \Gamma_n$ , the neutron branching  $\Gamma_n/\Gamma$  can be written as

$$\frac{\Gamma_n}{\Gamma} = \frac{\omega\gamma_{(\alpha,n)}}{(2J+1)\Gamma_\alpha} \quad (7)$$

and

$$\omega\gamma_{(\alpha,\gamma)} + \omega\gamma_{(\alpha,n)} = (2J+1)\Gamma_\alpha. \quad (8)$$

TABLE VI. Optical parameters used in FRESKO for distorted wave Born approximation (DWBA) analysis of  $^{22}\text{Ne}(^6\text{Li}, d)^{26}\text{Mg}$ .

Reaction channel	V (MeV)	$r_{0R}$ (fm)	$a_R$ (fm)	$W_s$ (MeV)	$4W_D$ (MeV)	$r_{0I}$ (fm)	$a_I$ (fm)	$r_{0C}$ (fm)
$^{22}\text{Ne} + ^6\text{Li}$	109.50	1.33	0.81	51.30		1.53	0.88	1.23
$^{26}\text{Mg} + d$	72.90	1.16	0.76		8.10	1.34	0.56	1.30
$\alpha + d$	<sup>a</sup>		0.67	0.65				
final state	<sup>b</sup>		1.31	0.65				

<sup>a</sup>Adjusted to give the correct  $^6\text{Li}$  binding energy.

<sup>b</sup>Adjusted to give the correct final state binding energy.

The ( $^6\text{Li}, d$ ) angular distributions obtained using FRESKO were used to compute the relative  $\alpha$  spectroscopic factors ( $S_{\alpha(\text{rel})}$ ) using the following equation:

$$\frac{d\sigma_{\text{exp}}}{d\Omega} = S_{\alpha(\text{rel})} N \frac{d\sigma_{\text{DWBA}}}{d\Omega} \quad (9)$$

where  $N$  is the normalization constant. For ( $^6\text{Li}, d$ ) and ( $d, ^6\text{Li}$ ) reactions,  $N$  has been found [89] to be equal to 2.67 from a comparison of  $\alpha$ -transfer and  $\alpha$ -decay data [48]. The  $S_{\alpha(\text{rel})}$  values determined using the above equation were scaled by a factor of  $\sim 2$  to reproduce the  $\alpha$  width ( $\Gamma_\alpha$ ) corresponding to the lowest directly observed resonance at  $E_R = 702$  keV. The resulting alpha spectroscopic factors ( $S_\alpha$ ) were then used to determine the  $\alpha$  widths for the present measurement using

$$\Gamma_\alpha = S_\alpha \Gamma_{\text{sp}}, \quad (10)$$

where  $\Gamma_{\text{sp}}$  represent the single-particle widths calculated using the optical potential parameters listed in Table VI.

The resulting resonance parameters for the levels observed in the astrophysical region of interest have been listed in Table VIII.

The reaction rate for  $E_R = 702$  keV resonance can be calculated from the experimentally known resonance strengths [53,54] and the corresponding uncertainty in the rate is given by their respective errors. As mentioned in Sec. IV C, the uncertainty in spin assignment has no influence on the corresponding reaction rate.

The  $\alpha$  width for the  $E_R = 553$  keV resonance has been determined relative to the  $\alpha$  width of the  $E_R = 702$  keV resonance as described above. However, for both resonances the spin is not uniquely determined. While our data prefers  $1^-$  assignments for both states, a  $2^+$  assignment can not be excluded. For this reason,  $\Gamma_\alpha$  for all possible spin combinations were calculated, as shown in Table VIII. In addition, the ratio of  $\Gamma_n/\Gamma$  was determined for each spin combination using the respective  $\Gamma_\alpha$ s and the experimental upper limit for  $\omega\gamma_{(\alpha,n)}$  given by Jaeger *et al.* [54]. This ratio was found to be  $\lesssim 0.1$  for all cases. Hence,  $\omega\gamma_{(\alpha,\gamma)}$  for this state can be calculated using Eq. (4). For the final reaction rate calculation for the  $(\alpha,\gamma)$  channel, a spin of  $1^-$  was adopted for both the states. The main uncertainty in the reaction rate is due to the uncertainty in the spin assignment. Hence the high and low rates were calculated from the results of the alternative choices. For the  $(\alpha,n)$  channel, the upper bound of the reaction rate is determined by the experimental upper limit of Jaeger *et al.* For the median rate a 50% value of this limit was adopted. Independently of this choice, the  $\omega\gamma_{(\alpha,\gamma)}$  is significantly larger than  $\omega\gamma_{(\alpha,n)}$ .

Tables IX and X show the  $\alpha$  capture rates calculated for the present work using the resonance parameters listed in Table VIII along with the Longland *et al.* [88] and NACRE [34] rates to facilitate the comparison.

In Table IX, the median rate represents the recommended  $(\alpha,\gamma)$  rate determined using the contributions from the 336 keV ( $E_x = 10951$  keV), the 553 keV ( $E_x = 11167$  keV), and the 702 keV ( $E_x = 11317$  keV) resonances observed in the present work along with the other known resonances reported in the literature from the direct measurement of the  $^{22}\text{Ne}(\alpha,\gamma)^{26}\text{Mg}$

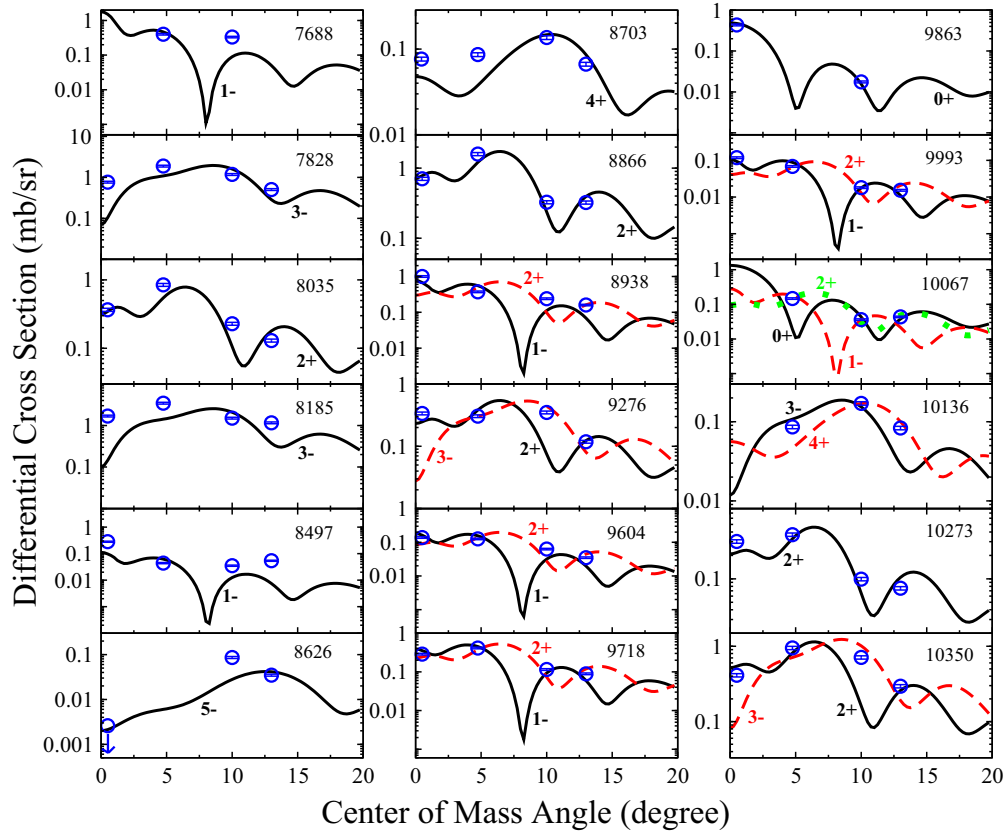


FIG. 5. Angular distributions obtained using PTOLEMY for states excited in the  $^{26}\text{Mg}(\alpha, \alpha')^{26}\text{Mg}$  reaction at  $E_\alpha = 206$  MeV. The blue circles with error bars represent the experimental data points. The empty blue circle with the blue arrow in the downward direction represents the upper limit for the cross section at that angle. The resulting spin-parities are based on present distributions and values quoted in literature.

reaction. The contribution from the 102 keV ( $E_x = 10717$  keV) resonance was negligible and hence has not been included in the rate calculation. The upper limit contributions from the 207 keV ( $E_x = 10822$  keV) and the  $2^+$  471 keV ( $E_x = 11085$  keV) resonances, seen only in the present ( $\alpha, \alpha'$ ) experiment, have been added to the high rate. The contribution from the 471 keV ( $E_x = 11085$  keV) resonance corresponding to the  $3^-$  angular distribution was added to the low rate.

In Table X, the median rate represents the recommended ( $\alpha, n$ ) rate determined using the contributions from the 553 keV ( $E_x = 11167$  keV) and the 702 keV ( $E_x = 11317$  keV) resonances observed in the present work along with the other known resonances reported in the literature from the direct measurement of the  $^{22}\text{Ne}(\alpha, n)^{25}\text{Mg}$  reaction.

Figure 8 depicts the behavior of the present  $^{22}\text{Ne}(\alpha, \gamma)^{26}\text{Mg}$  reaction rate with respect to temperature, corresponding to individual resonances observed in the astrophysical region of interest. Each rate has been normalized to the ( $\alpha, \gamma$ ) rate corresponding to the  $E_R = 702$  keV resonance, which is the lowest directly observed resonance. For  $T_9 < 0.18$ , the  $E_R = 336$  keV resonance ( $E_x = 10951$  keV) (blue dash-double-dotted line) has the largest contribution to the ( $\alpha, \gamma$ ) rate. However, for  $0.18 < T_9 < 0.4$ , the reaction rate corresponding to the  $E_R = 553$  keV resonance ( $E_x = 11167$  keV) (red solid line) dominates. The effect of this can also be seen in Fig. 9. The upper panel in Fig. 9 shows the comparison of the total

$^{22}\text{Ne}(\alpha, \gamma)^{26}\text{Mg}$  reaction rate calculated for the present work (red solid line) with that calculated by Longland *et al.* [88] (green long-dashed line), Bisterzo *et al.* [92] (blue dotted line) and NACRE [34] (black small-dashed line) along with the Hauser-Feshbach rates (NON-SMOKER) from the JINA Reaclib Database [91] (yellow dash-dotted line) and TALYS [93] (orange dash-double-dotted line). The lower panel shows the same comparison normalized to the NACRE total ( $\alpha, \gamma$ ) rate [34], to facilitate the comparison. Unlike the Bisterzo *et al.* data, all the other rates have adopted the Hauser-Feshbach rates, normalized to their respective experimental data, for temperatures approximately above 1.25 GK. For  $T_9 < 0.2$ , the present total ( $\alpha, \gamma$ ) rate is higher, by nearly up to 2 orders of magnitude, than the Longland *et al.* and Bisterzo *et al.* rates and almost by a factor of 3 larger than the NACRE rates. This is due to the large  $\alpha$  width associated with the  $E_R = 553$  keV resonance (as can be seen in Table VIII).

Figure 10 depicts the behavior of the present  $^{22}\text{Ne}(\alpha, n)^{25}\text{Mg}$  reaction rate with respect to temperature, corresponding to individual resonances observed above the  $n$  threshold. Each rate has been normalized to the ( $\alpha, n$ ) rate corresponding to the  $E_R = 702$  keV resonance, which is the lowest directly observed resonance. For  $T_9 < 0.22$ , the reaction rate corresponding to the  $E_R = 553$  keV resonance ( $E_x = 11167$  keV) (solid red line) dominates, above which the rate corresponding to the  $E_R = 702$  keV resonance

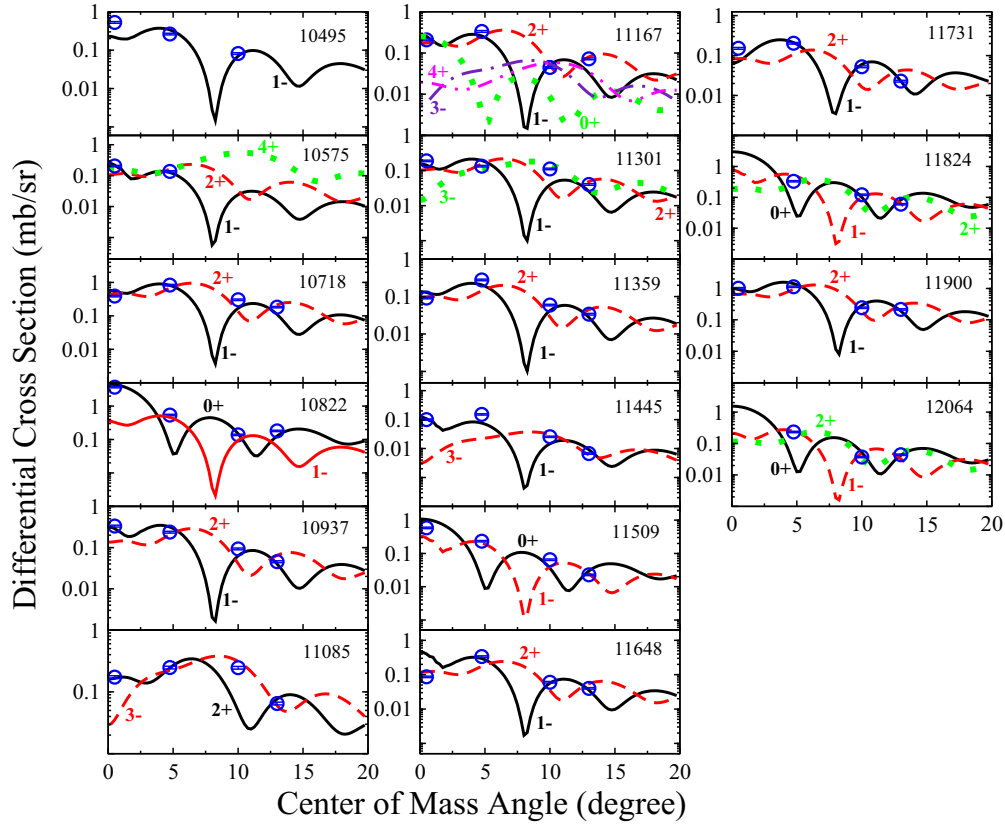


FIG. 6. Continuation of angular distributions obtained using PTOLEMY for states excited in the  $^{26}\text{Mg}(\alpha, \alpha')^{26}\text{Mg}$  reaction at  $E_\alpha = 206$  MeV. The blue circles with error bars represent the experimental data points. The resulting spin-parities are based on present distributions and values quoted in literature.

( $E_x = 11317$  keV) (green dash-dotted line) dominates. The same trend can be seen in Fig. 11, showing a similar comparison between the  $(\alpha, n)$  rates in the upper and lower panels as shown in Fig. 9 for the  $(\alpha, \gamma)$  rates.

The behavior of the  $^{22}\text{Ne}(\alpha, n)/^{22}\text{Ne}(\alpha, \gamma)$  reaction rate ratios is shown in Fig. 12. For  $T_9 < 0.5$ , the  $(\alpha, n)/(\alpha, \gamma)$  rate ratio in the present work (red solid line) is lower than those corresponding to the Longland *et al.* [88] (green long-dashed line), Bisterzo *et al.* [92] (blue dotted line), and NACRE [34] (black small-dashed line) rate ratios. This is because the  $\alpha$  width of the  $E_R = 553$  keV resonance ( $E_x = 11167$  keV) significantly increases the  $(\alpha, \gamma)$  rate such that for  $T_9 < 0.35$  the  $^{22}\text{Ne}(\alpha, \gamma)$  rate dominates over the  $^{22}\text{Ne}(\alpha, n)$  rate. This strongly indicates the need to study the influence of low energy resonances near the  $\alpha$  threshold on the  $\alpha$ -capture rates, which has been the primary objective of the present measurements.

### E. Astrophysical implications

As mentioned in Sec. I,  $^{22}\text{Ne}(\alpha, n)^{26}\text{Mg}$  is believed to be the main neutron source in massive stars and AGB stars of intermediate mass. In low mass AGB stars with solar-like metallicities, it is marginally activated during the advanced thermal pulses, giving rise to a small neutron exposure with a high peak neutron density [ $N_n(\text{peak}) \sim 10^{10} \text{ cm}^{-3}$ ]. As a consequence, the impact of  $^{22}\text{Ne} + \alpha$  capture rates on the whole  $s$ -process distribution is marginal in these models, with the

exception of a few isotopes involved in the branches of the  $s$  path. In the following paragraphs, a comparison of the effect of the present  $^{22}\text{Ne} + \alpha$  capture rates and literature rates on the  $s$ -process nucleosynthesis in these astrophysical scenarios is presented.

Figures 13, 14, 15, and 16 depict the impact of  $^{22}\text{Ne} + \alpha$  capture rates on isotopic overabundances of low and intermediate mass AGB stars. The overabundances signify the mass fractions ( $X_i$ ) over the solar-scaled initial values.

For a given AGB initial mass, the maximum temperature at the bottom of the convective zone increases as the metallicity decreases, and the  $^{22}\text{Ne}(\alpha, n)^{26}\text{Mg}$  source becomes more efficient. For a  $3M_\odot$  AGB model at  $[\text{Fe}/\text{H}] = -1$ , the maximum temperature at the bottom of the advanced thermal pulses reaches  $T_9 \sim 0.3$ . In the present scenario, both  $^{22}\text{Ne}(\alpha, n)^{26}\text{Mg}$  and  $^{13}\text{C}(\alpha, n)^{16}\text{O}$  neutron sources compete. The resulting variations in the overabundances are nevertheless small, as can be seen in Fig. 13, because the contribution of  $^{13}\text{C}(\alpha, n)^{16}\text{O}$  dominates.

For a  $5M_\odot$  AGB model at  $[\text{Fe}/\text{H}] = -0.3$ , higher temperatures are readily achieved at the bottom of the thermal pulses ( $T_9 \approx 0.35$ ). As a result, the  $^{22}\text{Ne}(\alpha, n)^{26}\text{Mg}$  reaction is efficiently activated, producing higher peak neutron densities of  $\approx 10^{11} \text{ cm}^{-3}$ . However, as can be seen in Fig. 9, the present recommended  $(\alpha, \gamma)$  rate is larger than that recommended by NACRE and Longland *et al.* Hence, it strongly competes with the  $(\alpha, n)$  neutron source leading to a decrease in the

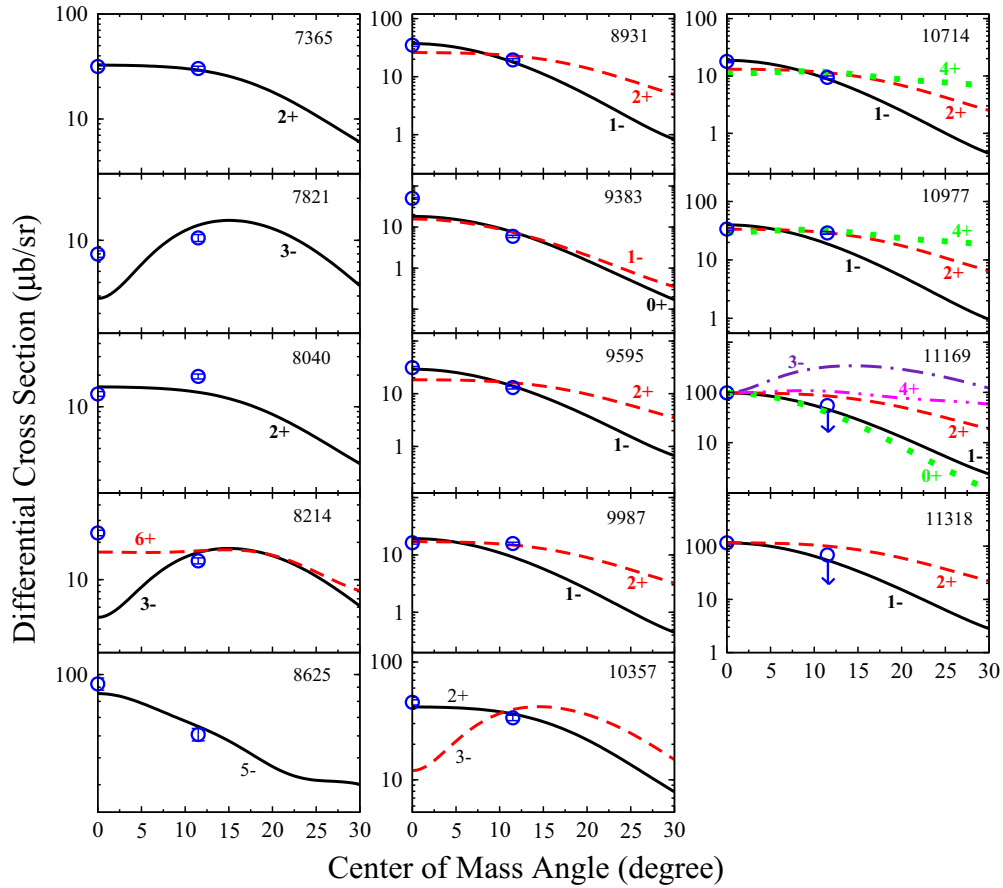


FIG. 7. Angular distributions obtained using FRESKO for states excited in the  $^{22}\text{Ne}(^6\text{Li}, d)^{26}\text{Mg}$  reaction at  $E_{\text{Li}} = 82.7$  MeV. The blue circles with error bars represent the experimental data points. The empty blue circles with the blue arrows in the downward direction represent the upper limit for the cross section at that angle. The resulting spin-parities are based on present distributions and values quoted in literature.

overabundances corresponding to the present work, as shown in Fig. 14.

Figures 17, 18, and 19 illustrate the impact of  $^{22}\text{Ne} + \alpha$  capture rates on the isotopic overabundance for a  $25M_{\odot}$ ,  $Z = 0.02$  massive star which includes contribution from both the convective core He burning as well as from the He-core ashes in the convective C-burning shell. However, as has been discussed in Sec. I, under C-burning conditions in massive stars, the  $^{22}\text{Ne}(p, \gamma)^{23}\text{Na}$  reaction becomes the main competitor of the

$^{22}\text{Ne}$  neutron source instead of the  $^{22}\text{Ne}(\alpha, \gamma)^{26}\text{Mg}$  reaction. Hence, the present  $(\alpha, \gamma)$  rates do not change the overall contribution coming from C burning. In all these figures,  $E_i/E_{\text{sun}}$  represents the elemental overabundance with respect to the solar abundance. The weak  $s$ -process region is between Fe and Sr-Y-Zr, where there is high production efficiency. As can be seen in Figs. 9 and 12, the present recommended  $(\alpha, \gamma)$  rate at  $T_9 = 0.3$  is stronger than the corresponding Longland *et al.* and NACRE rates. Hence, it strongly impacts the

TABLE VII. Spin-parity assignments for states populated above the  $\alpha$ -threshold in the present  $(\alpha, \alpha')$  and  $(^6\text{Li}, d)$  experiments.

$E_x$ (keV)	$E_R$ (keV)	$J^{\pi}$				
		Present work		Longland <i>et al.</i> [61]	Giesen <i>et al.</i> [48]	Adopted value(s)
		$^{26}\text{Mg}(\alpha, \alpha')^{26}\text{Mg}$	$^{22}\text{Ne}(^6\text{Li}, d)^{26}\text{Mg}$	$^{26}\text{Mg}(\gamma, \gamma')^{26}\text{Mg}$	$^{22}\text{Ne}(^6\text{Li}, d)^{26}\text{Mg}$	
10717(9)	102	$1^-, 2^+$	$1^-, 2^+, 4^+$		$4^+, 7^-, 8^+$	$1^-, 2^+$
10822(10)	207	$0^+, 1^-$		$1^-$		$1^-$
10951(21)	336	$1^-, 2^+$	$1^-, 2^+, 4^+$	$1^-$	$(2^+, 4^+), 3^-$	$1^-$
11085(8)	471	$2^+, 3^-$				$2^+, 3^-$
11167(8)	553	$1^-, 2^+$	$1^-^a$			$1^- (2^+)$
11317(18)	702		$1^-^a$		$(1^-), 2^+$	$1^- (2^+)$

<sup>a</sup>These values are based on the upper limit for the  $(^6\text{Li}, d)$  cross-section determined at  $10^\circ$ .

TABLE VIII. Resonance parameters for the  $^{26}\text{Mg}$  resonances observed in the present measurements in the astrophysical region of interest. The  $S_\alpha$  values listed here were obtained by scaling the relative  $\alpha$ -spectroscopic factors ( $S_{\alpha(\text{rel})}$ ) by a factor of  $\sim 2$ , as explained in Sec. IV D. The numbers in parenthesis are the uncertainties in the last digits of the corresponding values.

$E_x$ (keV)	$E_R^{\text{c.m.}}$ (keV)	$J^\pi$	$S_\alpha$	$\Gamma_{\text{sp}}$ (eV)	$(2J+1)\Gamma_\alpha$ (eV)	$\omega\gamma_{(\alpha,\gamma)}$ (eV)	$\omega\gamma_{(\alpha,n)}$ (eV)
10717(9)	102	$1^-$	0.07	$3.78 \times 10^{-35}$	$7.6(9) \times 10^{-36}$	$7.6(9) \times 10^{-36}$	
		$2^+$	0.13	$6.00 \times 10^{-36}$	$4(2) \times 10^{-36}$	$4(2) \times 10^{-36}$	
10822(10) <sup>a</sup>	207	$1^-$	$\leq 0.06$	$\leq 2.04 \times 10^{-20}$	$\leq 3.64 \times 10^{-21}$	$\leq 3.64 \times 10^{-21}$	
10951(21)	336	$1^-$	0.15	$5.68 \times 10^{-13}$	$2(1) \times 10^{-13}$	$2(1) \times 10^{-13}$	
11085(8) <sup>a</sup>	471	$2^+$	$\leq 0.06$	$\leq 9.75 \times 10^{-11}$	$\leq 2.95 \times 10^{-11}$	$\leq 2.95 \times 10^{-11}$	
		$3^-$	$\leq 0.07$	$\leq 1.36 \times 10^{-11}$	$\leq 6.20 \times 10^{-12}$	$\leq 6.20 \times 10^{-12}$	
11167(8)	553	$1^-$ <sup>e</sup>	0.36	$5.00 \times 10^{-07}$	$5.4(7) \times 10^{-07f}$	$5.4(7) \times 10^{-07}$	$6 \times 10^{-08b}$
		$2^+$	0.99	$8.78 \times 10^{-08}$	$4.4(5) \times 10^{-07f}$	$4.4(5) \times 10^{-07}$	$6 \times 10^{-08b}$
		$1^-$	0.44	$5.00 \times 10^{-07}$	$6.6(9) \times 10^{-07g}$	$6.6(9) \times 10^{-07}$	$6 \times 10^{-08b}$
		$2^+$	1.21	$8.78 \times 10^{-08}$	$5.3(7) \times 10^{-07g}$	$5.3(7) \times 10^{-07}$	$6 \times 10^{-08b}$
11317(18)	702	$1^-$ <sup>e</sup>	0.43	$1.18 \times 10^{-04}$	$1.5(2) \times 10^{-04d}$	$3.7(4) \times 10^{-05c}$	$1.2(1) \times 10^{-04c}$
		$2^+$	1.44	$2.15 \times 10^{-05}$	$1.5(2) \times 10^{-04d}$	$3.7(4) \times 10^{-05c}$	$1.2(1) \times 10^{-04c}$

<sup>a</sup>These peaks have not been seen in  $^{22}\text{Ne}(^6\text{Li},d)^{26}\text{Mg}$  spectra. However they were seen in  $^{26}\text{Mg}(\alpha,\alpha')^{26}\text{Mg}$  spectra. Hence, using kinematics, their positions were determined in the  $(^6\text{Li},d)$  spectra and upper limits for their corresponding resonance parameters were determined.

<sup>b</sup>This value is the upper limit predicted by Jaeger *et al.* [54].

<sup>c</sup>These values have been adopted from [53,54].

<sup>d</sup>These values have been calculated from the experimental resonance strengths [53,54].

<sup>e</sup>Adopted spin and parity.

<sup>f</sup> $\Gamma_\alpha$  determined assuming  $1^-$  spin and parity for the  $E_x = 11317$  keV state.

<sup>g</sup> $\Gamma_\alpha$  determined assuming  $2^+$  spin and parity for the  $E_x = 11317$  keV state.

availability of  $^{22}\text{Ne}$  for the  $s$  process in He-burning conditions, thereby showing a decrease in the overabundances for the present rates shown in Figs. 17 and 18.

The low rates and high rates associated with the median (recommended)  $^{22}\text{Ne} + \alpha$  capture rates in Tables IX and X translate into the resulting uncertainties associated with the  $s$ -process distribution shown in Figs. 15, 16, and 19. Figures 15 and 16 illustrate the uncertainty regions in the  $5M_\odot$  AGB star for different combinations of present  $(\alpha,n)$  lower and upper limits, present  $(\alpha,\gamma)$  median rates, and lower and upper limits. Figure 19 illustrates the uncertainty band for the present work (green area) along with that corresponding to Longland *et al.* (blue area) in a  $25M_\odot$  massive star for the  $^{22}\text{Ne}(\alpha,n)$  high to  $^{22}\text{Ne}(\alpha,\gamma)$  low range and for the  $^{22}\text{Ne}(\alpha,n)$  low to  $^{22}\text{Ne}(\alpha,\gamma)$  high range.

In all these figures, the present  $^{22}\text{Ne}(\alpha,n) + ^{22}\text{Ne}(\alpha,\gamma)$  rates strongly favor the reduction of  $s$ -process overabundances associated with massive stars as well as AGB stars of intermediate initial mass. This is due to the large  $\alpha$  width associated with  $E_x = 11167$  keV state, which significantly increases the  $(\alpha,\gamma)$  rate, thereby reducing the efficiency of the  $(\alpha,n)$  rate.

## V. CONCLUSIONS

The goal of this study was to investigate the nuclear structure of  $^{26}\text{Mg}$  and determine the  $\alpha$  widths for the resonances observed above the  $\alpha$  threshold. This nucleus is the compound nucleus that is formed during  $\alpha$ -capture reactions on  $^{22}\text{Ne}$  that is predicted to serve as the primary neutron source for the  $s$  process in massive stars and intermediate mass AGB stars.

In the present work, six resonances have been observed above the  $\alpha$  threshold, with four [ $E_x = 10717(9)$ ,  $10822(10)$ ,  $10951(21)$ , and  $11085(8)$  keV] between the  $\alpha$  and  $n$  thresholds and two [ $E_x = 11167(8)$  and  $11317(18)$  keV] above the  $n$  threshold.

Among the six observed resonances, the  $E_x = 10951$ ,  $11167$ , and  $11317$  keV states exhibited pronounced  $\alpha$ -cluster structures, as reflected by their large  $\alpha$ -spectroscopic factors (Table VIII). Hence, these resonances dominated the  $\alpha$ -capture rates with the  $E_x = 11167$  keV state increasing the  $(\alpha,\gamma)$  rate by nearly up to 2 orders of magnitude above the Longland *et al.* [88] and Bisterzo *et al.* [92] rates and almost by a factor of 3 above the NACRE rates [34] for  $T_9 < 0.2$ . The rate contributions corresponding to the  $E_x = 10822$  and  $11085$  keV states were included in the uncertainty calculations since these resonances were observed only in the  $(\alpha,\alpha')$  measurement.

A similar trend was seen in the  $s$ -process elemental distribution. The present  $^{22}\text{Ne}(\alpha,n) + ^{22}\text{Ne}(\alpha,\gamma)$  rates favored reduced  $s$ -process overabundances in massive stars and intermediate mass AGB stars where  $T_9 \geq 0.3$  is readily achieved to activate the  $^{22}\text{Ne}$  neutron source. On the other hand, in low mass AGB stars, where such high temperatures are reached only during the last few thermal pulses, the  $s$ -process overabundances corresponding to the present rates did not show much variation compared to the literature rates.

All in all, the recommended  $^{22}\text{Ne} + \alpha$  capture rates, determined in the present measurements, strongly suggest a reduction in the number of  $^{22}\text{Ne}$  nuclei available for neutron production, thereby lowering the  $s$ -process overabundances. However, the associated uncertainties point toward the need to better constrain the resonance parameters in order to establish

TABLE IX. Monte Carlo reaction rates for the  $^{22}\text{Ne}(\alpha, \gamma)^{26}\text{Mg}$  reaction calculated using the nucleosynthesis simulator called STARLIB [90]. The rate values in parenthesis represent the temperatures ( $T_9 > T_{9\text{match}} = 1.5$ ) for which the NON-SMOKER Hauser Feshbach rates from the JINA Reaclib Database [91], normalized to the experimental results, have been adopted. The Longland *et al.* [88] and NACRE [34] rates have also been provided to facilitate the comparison.

$T_9$	Present work			Longland <i>et al.</i> [88]			NACRE [34]		
	Low rate	Median rate	High rate	Low rate	Median rate	High rate	Low rate	Median rate	High rate
0.01	$4.85 \times 10^{-81}$	$6.18 \times 10^{-81}$	$7.98 \times 10^{-81}$	$1.05 \times 10^{-77}$	$2.14 \times 10^{-77}$	$4.52 \times 10^{-77}$	0.00	0.00	0.00
0.011	$4.20 \times 10^{-78}$	$5.36 \times 10^{-78}$	$6.92 \times 10^{-78}$	$3.99 \times 10^{-74}$	$7.28 \times 10^{-74}$	$1.34 \times 10^{-73}$	0.00	0.00	0.00
0.012	$1.68 \times 10^{-75}$	$2.14 \times 10^{-75}$	$2.76 \times 10^{-75}$	$3.69 \times 10^{-71}$	$6.34 \times 10^{-71}$	$1.07 \times 10^{-70}$	0.00	0.00	0.00
0.013	$3.56 \times 10^{-73}$	$4.54 \times 10^{-73}$	$5.86 \times 10^{-73}$	$1.15 \times 10^{-68}$	$1.90 \times 10^{-68}$	$3.09 \times 10^{-68}$	0.00	0.00	0.00
0.014	$4.47 \times 10^{-71}$	$5.71 \times 10^{-71}$	$7.37 \times 10^{-71}$	$1.55 \times 10^{-66}$	$2.52 \times 10^{-66}$	$4.04 \times 10^{-66}$	0.00	0.00	0.00
0.015	$3.62 \times 10^{-69}$	$4.62 \times 10^{-69}$	$5.96 \times 10^{-69}$	$1.06 \times 10^{-64}$	$1.73 \times 10^{-64}$	$2.79 \times 10^{-64}$	0.00	0.00	0.00
0.016	$2.01 \times 10^{-67}$	$2.57 \times 10^{-67}$	$3.31 \times 10^{-67}$	$4.11 \times 10^{-63}$	$6.96 \times 10^{-63}$	$1.14 \times 10^{-62}$	0.00	0.00	0.00
0.018	$2.47 \times 10^{-64}$	$3.15 \times 10^{-64}$	$4.07 \times 10^{-64}$	$1.80 \times 10^{-60}$	$3.26 \times 10^{-60}$	$5.63 \times 10^{-60}$	0.00	0.00	0.00
0.02	$1.13 \times 10^{-61}$	$1.45 \times 10^{-61}$	$1.87 \times 10^{-61}$	$2.24 \times 10^{-58}$	$4.34 \times 10^{-58}$	$8.04 \times 10^{-58}$	0.00	0.00	0.00
0.025	$2.46 \times 10^{-56}$	$3.14 \times 10^{-56}$	$4.04 \times 10^{-56}$	$1.54 \times 10^{-54}$	$3.14 \times 10^{-54}$	$6.30 \times 10^{-54}$	0.00	0.00	0.00
0.03	$2.91 \times 10^{-52}$	$3.71 \times 10^{-52}$	$4.77 \times 10^{-52}$	$2.82 \times 10^{-50}$	$3.35 \times 10^{-49}$	$1.30 \times 10^{-48}$	0.00	0.00	0.00
0.04	$2.62 \times 10^{-46}$	$3.38 \times 10^{-46}$	$4.60 \times 10^{-46}$	$1.81 \times 10^{-42}$	$2.31 \times 10^{-41}$	$8.91 \times 10^{-41}$	0.00	0.00	0.00
0.05	$8.78 \times 10^{-42}$	$6.82 \times 10^{-41}$	$1.34 \times 10^{-39}$	$8.51 \times 10^{-38}$	$1.08 \times 10^{-36}$	$4.17 \times 10^{-36}$	0.00	0.00	0.00
0.06	$2.23 \times 10^{-36}$	$2.11 \times 10^{-35}$	$2.05 \times 10^{-34}$	$1.05 \times 10^{-34}$	$1.34 \times 10^{-33}$	$5.14 \times 10^{-33}$	0.00	0.00	0.00
0.07	$3.33 \times 10^{-32}$	$1.82 \times 10^{-31}$	$1.01 \times 10^{-30}$	$1.95 \times 10^{-32}$	$2.12 \times 10^{-31}$	$8.04 \times 10^{-31}$	0.00	0.00	0.00
0.08	$4.33 \times 10^{-29}$	$1.54 \times 10^{-28}$	$6.03 \times 10^{-28}$	$2.76 \times 10^{-30}$	$1.14 \times 10^{-29}$	$3.67 \times 10^{-29}$	0.00	0.00	0.00
0.09	$1.09 \times 10^{-26}$	$2.86 \times 10^{-26}$	$8.58 \times 10^{-26}$	$1.76 \times 10^{-28}$	$6.30 \times 10^{-28}$	$1.35 \times 10^{-27}$	0.00	0.00	0.00
0.1	$8.63 \times 10^{-25}$	$1.81 \times 10^{-24}$	$4.49 \times 10^{-24}$	$4.79 \times 10^{-27}$	$2.28 \times 10^{-26}$	$6.55 \times 10^{-26}$	0.00	0.00	0.00
0.11	$2.91 \times 10^{-23}$	$5.26 \times 10^{-23}$	$1.20 \times 10^{-22}$	$8.17 \times 10^{-26}$	$5.95 \times 10^{-25}$	$1.86 \times 10^{-24}$	0.00	0.00	0.00
0.12	$5.09 \times 10^{-22}$	$8.72 \times 10^{-22}$	$1.91 \times 10^{-21}$	$1.11 \times 10^{-24}$	$9.63 \times 10^{-24}$	$3.07 \times 10^{-23}$	$3.70 \times 10^{-23}$	$5.24 \times 10^{-22}$	$5.81 \times 10^{-21}$
0.13	$5.55 \times 10^{-21}$	$9.56 \times 10^{-21}$	$2.06 \times 10^{-20}$	$1.23 \times 10^{-23}$	$1.03 \times 10^{-22}$	$3.28 \times 10^{-22}$	$4.10 \times 10^{-22}$	$5.77 \times 10^{-21}$	$6.32 \times 10^{-20}$
0.14	$4.31 \times 10^{-20}$	$7.58 \times 10^{-20}$	$1.63 \times 10^{-19}$	$1.38 \times 10^{-22}$	$8.23 \times 10^{-22}$	$2.50 \times 10^{-21}$	$3.20 \times 10^{-21}$	$4.52 \times 10^{-20}$	$4.91 \times 10^{-19}$
0.15	$2.75 \times 10^{-19}$	$4.88 \times 10^{-19}$	$1.04 \times 10^{-18}$	$1.53 \times 10^{-21}$	$5.57 \times 10^{-21}$	$1.51 \times 10^{-20}$	$1.90 \times 10^{-20}$	$2.73 \times 10^{-19}$	$2.95 \times 10^{-18}$
0.16	$1.63 \times 10^{-18}$	$2.84 \times 10^{-18}$	$5.70 \times 10^{-18}$	$1.41 \times 10^{-20}$	$3.79 \times 10^{-20}$	$8.10 \times 10^{-20}$	$9.00 \times 10^{-20}$	$1.38 \times 10^{-18}$	$1.50 \times 10^{-17}$
0.18	$5.68 \times 10^{-17}$	$8.69 \times 10^{-17}$	$1.43 \times 10^{-16}$	$8.05 \times 10^{-19}$	$1.54 \times 10^{-18}$	$2.84 \times 10^{-18}$	$1.30 \times 10^{-18}$	$2.96 \times 10^{-17}$	$3.28 \times 10^{-16}$
0.2	$1.41 \times 10^{-15}$	$2.03 \times 10^{-15}$	$2.97 \times 10^{-15}$	$3.41 \times 10^{-17}$	$5.43 \times 10^{-17}$	$9.60 \times 10^{-17}$	$2.20 \times 10^{-17}$	$6.04 \times 10^{-16}$	$6.65 \times 10^{-15}$
0.25	$6.04 \times 10^{-13}$	$8.42 \times 10^{-13}$	$1.17 \times 10^{-12}$	$5.88 \times 10^{-14}$	$7.56 \times 10^{-14}$	$1.00 \times 10^{-13}$	$3.40 \times 10^{-14}$	$3.12 \times 10^{-13}$	$3.01 \times 10^{-12}$
0.3	$3.70 \times 10^{-11}$	$5.20 \times 10^{-11}$	$7.30 \times 10^{-11}$	$9.32 \times 10^{-12}$	$1.13 \times 10^{-11}$	$1.38 \times 10^{-11}$	$5.90 \times 10^{-12}$	$2.56 \times 10^{-11}$	$2.03 \times 10^{-10}$
0.35	$7.47 \times 10^{-10}$	$1.07 \times 10^{-9}$	$1.54 \times 10^{-9}$	$3.46 \times 10^{-10}$	$4.08 \times 10^{-10}$	$4.86 \times 10^{-10}$	$2.30 \times 10^{-10}$	$6.58 \times 10^{-10}$	$4.23 \times 10^{-9}$
0.4	$7.58 \times 10^{-9}$	$1.11 \times 10^{-8}$	$1.62 \times 10^{-8}$	$5.11 \times 10^{-9}$	$5.95 \times 10^{-9}$	$6.98 \times 10^{-9}$	$3.49 \times 10^{-9}$	$7.89 \times 10^{-9}$	$4.21 \times 10^{-8}$
0.45	$4.86 \times 10^{-8}$	$7.10 \times 10^{-8}$	$1.03 \times 10^{-7}$	$4.09 \times 10^{-8}$	$4.72 \times 10^{-8}$	$5.50 \times 10^{-8}$	$2.84 \times 10^{-8}$	$5.56 \times 10^{-8}$	$2.54 \times 10^{-7}$
0.5	$2.22 \times 10^{-7}$	$3.22 \times 10^{-7}$	$4.65 \times 10^{-7}$	$2.13 \times 10^{-7}$	$2.44 \times 10^{-7}$	$2.82 \times 10^{-7}$	$1.49 \times 10^{-7}$	$2.67 \times 10^{-7}$	$1.08 \times 10^{-6}$
0.6	$2.27 \times 10^{-6}$	$3.20 \times 10^{-6}$	$4.46 \times 10^{-6}$	$2.47 \times 10^{-6}$	$2.79 \times 10^{-6}$	$3.20 \times 10^{-6}$	$1.74 \times 10^{-6}$	$2.80 \times 10^{-6}$	$9.49 \times 10^{-6}$
0.7	$1.23 \times 10^{-5}$	$1.67 \times 10^{-5}$	$2.25 \times 10^{-5}$	$1.39 \times 10^{-5}$	$1.57 \times 10^{-5}$	$1.78 \times 10^{-5}$	$9.90 \times 10^{-6}$	$1.49 \times 10^{-5}$	$4.48 \times 10^{-5}$
0.8	$4.57 \times 10^{-5}$	$5.92 \times 10^{-5}$	$7.69 \times 10^{-5}$	$5.15 \times 10^{-5}$	$5.77 \times 10^{-5}$	$6.51 \times 10^{-5}$	$3.69 \times 10^{-5}$	$5.30 \times 10^{-5}$	$1.44 \times 10^{-4}$
0.9	$1.34 \times 10^{-4}$	$1.68 \times 10^{-4}$	$2.10 \times 10^{-4}$	$1.48 \times 10^{-4}$	$1.66 \times 10^{-4}$	$1.88 \times 10^{-4}$	$1.08 \times 10^{-4}$	$1.49 \times 10^{-4}$	$3.65 \times 10^{-4}$
1	$3.40 \times 10^{-4}$	$4.17 \times 10^{-4}$	$5.14 \times 10^{-4}$	$3.65 \times 10^{-4}$	$4.11 \times 10^{-4}$	$4.73 \times 10^{-4}$	$2.73 \times 10^{-4}$	$3.63 \times 10^{-4}$	$7.95 \times 10^{-4}$
1.25	$2.31 \times 10^{-3}$	$2.85 \times 10^{-3}$	$3.69 \times 10^{-3}$	$2.33 \times 10^{-3}$	$2.77 \times 10^{-3}$	$3.43 \times 10^{-3}$	$1.81 \times 10^{-3}$	$2.41 \times 10^{-3}$	$4.02 \times 10^{-3}$
1.5	$1.03 \times 10^{-2}$	$1.32 \times 10^{-2}$	$1.77 \times 10^{-2}$	$(1.45 \times 10^{-2})$	$(1.79 \times 10^{-2})$	$(2.21 \times 10^{-2})$	$1.17 \times 10^{-2}$	$1.57 \times 10^{-2}$	$2.64 \times 10^{-2}$
2	$(1.71 \times 10^{-1})$	$(2.18 \times 10^{-1})$	$(2.91 \times 10^{-1})$	$(3.00 \times 10^{-1})$	$(3.70 \times 10^{-1})$	$(4.58 \times 10^{-1})$	$2.11 \times 10^{-1}$	$2.90 \times 10^{-1}$	$5.01 \times 10^{-1}$
2.5	$(1.35 \times 10^{00})$	$(1.73 \times 10^{00})$	$(2.31 \times 10^{00})$	$(2.55 \times 10^{00})$	$(3.15 \times 10^{00})$	$(3.89 \times 10^{00})$	$1.66 \times 10^{00}$	$2.33 \times 10^{00}$	$4.12 \times 10^{00}$
3	$(6.54 \times 10^{00})$	$(8.37 \times 10^{00})$	$(1.12 \times 10^{01})$	$(1.24 \times 10^{01})$	$(1.53 \times 10^{01})$	$(1.89 \times 10^{01})$	$7.40 \times 10^{00}$	$1.07 \times 10^{01}$	$1.94 \times 10^{01}$
3.5	$(2.24 \times 10^{01})$	$(2.87 \times 10^{01})$	$(3.83 \times 10^{01})$	$(4.18 \times 10^{01})$	$(5.17 \times 10^{01})$	$(6.39 \times 10^{01})$	$2.34 \times 10^{01}$	$3.44 \times 10^{01}$	$6.42 \times 10^{01}$
4	$(6.02 \times 10^{01})$	$(7.70 \times 10^{01})$	$(1.03 \times 10^{02})$	$(1.10 \times 10^{02})$	$(1.36 \times 10^{02})$	$(1.68 \times 10^{02})$	$5.83 \times 10^{01}$	$8.84 \times 10^{01}$	$1.69 \times 10^{02}$
5	$(2.65 \times 10^{02})$	$(3.40 \times 10^{02})$	$(4.53 \times 10^{02})$	$(4.71 \times 10^{02})$	$(5.82 \times 10^{02})$	$(7.19 \times 10^{02})$	$2.29 \times 10^{02}$	$3.69 \times 10^{02}$	$7.46 \times 10^{02}$
6	$(7.65 \times 10^{02})$	$(9.80 \times 10^{02})$	$(1.31 \times 10^{03})$	$(1.33 \times 10^{03})$	$(1.64 \times 10^{03})$	$(2.03 \times 10^{03})$	$5.90 \times 10^{02}$	$1.02 \times 10^{03}$	$2.19 \times 10^{03}$
7	$(1.69 \times 10^{03})$	$(2.17 \times 10^{03})$	$(2.89 \times 10^{03})$	$(2.91 \times 10^{03})$	$(3.59 \times 10^{03})$	$(4.44 \times 10^{03})$	$1.14 \times 10^{03}$	$2.17 \times 10^{03}$	$4.95 \times 10^{03}$
8	$(3.13 \times 10^{03})$	$(4.01 \times 10^{03})$	$(5.35 \times 10^{03})$	$(5.35 \times 10^{03})$	$(6.62 \times 10^{03})$	$(8.18 \times 10^{03})$	$1.78 \times 10^{03}$	$3.83 \times 10^{03}$	$9.32 \times 10^{03}$
9	$(5.10 \times 10^{03})$	$(6.54 \times 10^{03})$	$(8.72 \times 10^{03})$	$(8.68 \times 10^{03})$	$(1.07 \times 10^{04})$	$(1.33 \times 10^{04})$	$2.36 \times 10^{03}$	$5.92 \times 10^{03}$	$1.55 \times 10^{04}$
10	$(7.54 \times 10^{03})$	$(9.65 \times 10^{03})$	$(1.29 \times 10^{04})$	$(1.30 \times 10^{04})$	$(1.60 \times 10^{04})$	$(1.98 \times 10^{04})$	$2.67 \times 10^{03}$	$8.31 \times 10^{03}$	$2.34 \times 10^{04}$

TABLE X. Monte Carlo reaction rates for the  $^{22}\text{Ne}(\alpha,n)^{25}\text{Mg}$  reaction calculated using the nucleosynthesis simulator called STARLIB [90]. The rate values in parenthesis represent the temperatures ( $T_9 > T_{9\text{match}} = 1.5$ ) for which NON-SMOKER Hauser Feshbach rates from the JINA Reaclib Database [91], normalized to the experimental results, have been adopted. The Longland *et al.* [88] and NACRE [34] rates have also been provided to facilitate the comparison.

$T_9$	Present work			Longland <i>et al.</i> [88]			NACRE [34]		
	Low rate	Median rate	High rate	Low rate	Median rate	High rate	Low rate	Median rate	High rate
0.01	$6.97 \times 10^{-252}$	$7.87 \times 10^{-252}$	$8.86 \times 10^{-252}$	0.00	0.00	0.00	0.00	0.00	0.00
0.011	$6.65 \times 10^{-230}$	$7.50 \times 10^{-230}$	$8.45 \times 10^{-230}$	0.00	0.00	0.00	0.00	0.00	0.00
0.012	$1.39 \times 10^{-211}$	$1.57 \times 10^{-211}$	$1.77 \times 10^{-211}$	0.00	0.00	0.00	0.00	0.00	0.00
0.013	$4.34 \times 10^{-196}$	$4.90 \times 10^{-196}$	$5.51 \times 10^{-196}$	0.00	0.00	0.00	0.00	0.00	0.00
0.014	$8.47 \times 10^{-183}$	$9.56 \times 10^{-183}$	$1.08 \times 10^{-182}$	0.00	0.00	0.00	0.00	0.00	0.00
0.015	$2.81 \times 10^{-171}$	$3.17 \times 10^{-171}$	$3.57 \times 10^{-171}$	0.00	0.00	0.00	0.00	0.00	0.00
0.016	$3.40 \times 10^{-161}$	$3.84 \times 10^{-161}$	$4.32 \times 10^{-161}$	0.00	0.00	0.00	0.00	0.00	0.00
0.018	$2.20 \times 10^{-144}$	$2.48 \times 10^{-144}$	$2.79 \times 10^{-144}$	0.00	0.00	0.00	0.00	0.00	0.00
0.02	$6.26 \times 10^{-131}$	$7.07 \times 10^{-131}$	$7.96 \times 10^{-131}$	0.00	0.00	0.00	0.00	0.00	0.00
0.025	$1.09 \times 10^{-106}$	$1.23 \times 10^{-106}$	$1.38 \times 10^{-106}$	0.00	0.00	0.00	0.00	0.00	0.00
0.03	$1.66 \times 10^{-90}$	$1.88 \times 10^{-90}$	$2.11 \times 10^{-90}$	$5.12 \times 10^{-88}$	$5.08 \times 10^{-87}$	$2.25 \times 10^{-86}$	0.00	0.00	0.00
0.04	$3.16 \times 10^{-70}$	$3.77 \times 10^{-70}$	$4.44 \times 10^{-70}$	$1.46 \times 10^{-67}$	$1.49 \times 10^{-66}$	$6.64 \times 10^{-66}$	0.00	0.00	0.00
0.05	$5.19 \times 10^{-58}$	$1.88 \times 10^{-57}$	$3.25 \times 10^{-57}$	$2.99 \times 10^{-55}$	$3.05 \times 10^{-54}$	$1.36 \times 10^{-53}$	0.00	0.00	0.00
0.06	$7.89 \times 10^{-50}$	$1.99 \times 10^{-48}$	$3.89 \times 10^{-48}$	$4.92 \times 10^{-47}$	$4.87 \times 10^{-46}$	$2.17 \times 10^{-45}$	0.00	0.00	0.00
0.07	$5.94 \times 10^{-44}$	$6.52 \times 10^{-42}$	$1.30 \times 10^{-41}$	$3.70 \times 10^{-41}$	$3.48 \times 10^{-40}$	$1.55 \times 10^{-39}$	0.00	0.00	0.00
0.08	$1.63 \times 10^{-39}$	$5.00 \times 10^{-37}$	$9.98 \times 10^{-37}$	$1.03 \times 10^{-36}$	$8.44 \times 10^{-36}$	$3.73 \times 10^{-35}$	0.00	0.00	0.00
0.09	$4.99 \times 10^{-36}$	$3.09 \times 10^{-33}$	$6.17 \times 10^{-33}$	$3.23 \times 10^{-33}$	$2.19 \times 10^{-32}$	$9.43 \times 10^{-32}$	0.00	0.00	0.00
0.1	$3.39 \times 10^{-33}$	$3.28 \times 10^{-30}$	$6.56 \times 10^{-30}$	$2.17 \times 10^{-30}$	$1.20 \times 10^{-29}$	$4.92 \times 10^{-29}$	0.00	0.00	0.00
0.11	$8.14 \times 10^{-31}$	$9.69 \times 10^{-28}$	$1.94 \times 10^{-27}$	$4.65 \times 10^{-28}$	$2.12 \times 10^{-27}$	$8.22 \times 10^{-27}$	0.00	0.00	0.00
0.12	$1.06 \times 10^{-28}$	$1.10 \times 10^{-25}$	$2.20 \times 10^{-25}$	$4.24 \times 10^{-26}$	$1.62 \times 10^{-25}$	$5.82 \times 10^{-25}$	$1.00 \times 10^{-26}$	$2.33 \times 10^{-25}$	$1.20 \times 10^{-22}$
0.13	$1.06 \times 10^{-26}$	$5.96 \times 10^{-24}$	$1.20 \times 10^{-23}$	$1.94 \times 10^{-24}$	$6.61 \times 10^{-24}$	$2.14 \times 10^{-23}$	$4.00 \times 10^{-25}$	$8.64 \times 10^{-24}$	$5.37 \times 10^{-21}$
0.14	$7.56 \times 10^{-25}$	$1.83 \times 10^{-22}$	$3.73 \times 10^{-22}$	$5.27 \times 10^{-23}$	$1.64 \times 10^{-22}$	$4.81 \times 10^{-22}$	$1.10 \times 10^{-23}$	$1.96 \times 10^{-22}$	$1.44 \times 10^{-19}$
0.15	$3.42 \times 10^{-23}$	$3.57 \times 10^{-21}$	$7.42 \times 10^{-21}$	$9.94 \times 10^{-22}$	$2.74 \times 10^{-21}$	$7.18 \times 10^{-21}$	$2.60 \times 10^{-22}$	$3.03 \times 10^{-21}$	$2.55 \times 10^{-18}$
0.16	$9.80 \times 10^{-22}$	$4.87 \times 10^{-20}$	$1.04 \times 10^{-19}$	$1.43 \times 10^{-20}$	$3.39 \times 10^{-20}$	$7.89 \times 10^{-20}$	$4.80 \times 10^{-21}$	$3.51 \times 10^{-20}$	$3.20 \times 10^{-17}$
0.18	$2.66 \times 10^{-19}$	$4.09 \times 10^{-18}$	$9.28 \times 10^{-18}$	$1.61 \times 10^{-18}$	$2.74 \times 10^{-18}$	$5.01 \times 10^{-18}$	$9.10 \times 10^{-19}$	$2.68 \times 10^{-18}$	$2.22 \times 10^{-15}$
0.2	$2.35 \times 10^{-17}$	$1.64 \times 10^{-16}$	$3.90 \times 10^{-16}$	$9.14 \times 10^{-17}$	$1.24 \times 10^{-16}$	$1.79 \times 10^{-16}$	$7.00 \times 10^{-17}$	$1.23 \times 10^{-16}$	$6.70 \times 10^{-14}$
0.25	$7.18 \times 10^{-14}$	$2.06 \times 10^{-13}$	$4.74 \times 10^{-13}$	$1.68 \times 10^{-13}$	$2.06 \times 10^{-13}$	$2.53 \times 10^{-13}$	$1.82 \times 10^{-13}$	$2.30 \times 10^{-13}$	$3.14 \times 10^{-11}$
0.3	$1.44 \times 10^{-11}$	$3.10 \times 10^{-11}$	$6.33 \times 10^{-11}$	$2.74 \times 10^{-11}$	$3.36 \times 10^{-11}$	$4.15 \times 10^{-11}$	$3.37 \times 10^{-11}$	$4.06 \times 10^{-11}$	$1.92 \times 10^{-9}$
0.35	$6.29 \times 10^{-10}$	$1.16 \times 10^{-9}$	$2.13 \times 10^{-9}$	$1.05 \times 10^{-9}$	$1.29 \times 10^{-9}$	$1.59 \times 10^{-9}$	$1.37 \times 10^{-9}$	$1.64 \times 10^{-9}$	$3.68 \times 10^{-8}$
0.4	$1.07 \times 10^{-8}$	$1.78 \times 10^{-8}$	$2.98 \times 10^{-8}$	$1.64 \times 10^{-8}$	$2.00 \times 10^{-8}$	$2.45 \times 10^{-8}$	$2.18 \times 10^{-8}$	$2.60 \times 10^{-8}$	$3.43 \times 10^{-7}$
0.45	$1.01 \times 10^{-7}$	$1.52 \times 10^{-7}$	$2.35 \times 10^{-7}$	$1.42 \times 10^{-7}$	$1.71 \times 10^{-7}$	$2.07 \times 10^{-7}$	$1.90 \times 10^{-7}$	$2.27 \times 10^{-7}$	$1.98 \times 10^{-6}$
0.5	$6.65 \times 10^{-7}$	$9.10 \times 10^{-7}$	$1.29 \times 10^{-6}$	$8.51 \times 10^{-7}$	$1.00 \times 10^{-6}$	$1.19 \times 10^{-6}$	$1.12 \times 10^{-6}$	$1.33 \times 10^{-6}$	$8.26 \times 10^{-6}$
0.6	$1.72 \times 10^{-5}$	$1.96 \times 10^{-5}$	$2.32 \times 10^{-5}$	$1.74 \times 10^{-5}$	$1.92 \times 10^{-5}$	$2.15 \times 10^{-5}$	$2.10 \times 10^{-5}$	$2.45 \times 10^5$	$7.97 \times 10^{-5}$
0.7	$2.79 \times 10^{-4}$	$2.93 \times 10^{-4}$	$3.11 \times 10^{-4}$	$2.36 \times 10^{-4}$	$2.51 \times 10^{-4}$	$2.69 \times 10^{-4}$	$2.67 \times 10^{-4}$	$3.04 \times 10^{-4}$	$5.60 \times 10^{-4}$
0.8	$2.76 \times 10^{-3}$	$2.85 \times 10^{-3}$	$2.95 \times 10^{-3}$	$2.15 \times 10^{-3}$	$2.27 \times 10^{-3}$	$2.42 \times 10^{-3}$	$2.39 \times 10^{-3}$	$2.69 \times 10^{-3}$	$3.63 \times 10^{-3}$
0.9	$1.79 \times 10^{-2}$	$1.85 \times 10^{-2}$	$1.91 \times 10^{-2}$	$1.36 \times 10^{-2}$	$1.43 \times 10^{-2}$	$1.51 \times 10^{-2}$	$1.50 \times 10^{-2}$	$1.68 \times 10^{-2}$	$2.00 \times 10^{-2}$
1	$8.36 \times 10^{-2}$	$8.68 \times 10^{-2}$	$9.00 \times 10^{-2}$	$6.34 \times 10^{-2}$	$6.64 \times 10^{-2}$	$6.98 \times 10^{-2}$	$6.99 \times 10^{-2}$	$7.81 \times 10^{-2}$	$8.91 \times 10^{-2}$
1.25	$1.51 \times 10^{00}$	$1.59 \times 10^{00}$	$1.68 \times 10^{00}$	$1.18 \times 10^{+00}$	$1.22 \times 10^{+00}$	$1.27 \times 10^{+00}$	$1.33 \times 10^{+00}$	$1.50 \times 10^{+00}$	$1.68 \times 10^{+00}$
1.5	$1.14 \times 10^{01}$	$1.22 \times 10^{01}$	$1.30 \times 10^{01}$	$(1.09 \times 10^{+01})$	$(1.14 \times 10^{+01})$	$(1.18 \times 10^{+01})$	$1.12 \times 10^{+01}$	$1.30 \times 10^{+01}$	$1.48 \times 10^{+01}$
2	$(3.09 \times 10^{02})$	$(3.30 \times 10^{02})$	$(3.54 \times 10^{02})$	$(2.92 \times 10^{+02})$	$(3.04 \times 10^{+02})$	$(3.16 \times 10^{+02})$	$2.22 \times 10^{+02}$	$2.76 \times 10^{+02}$	$3.30 \times 10^{+02}$
2.5	$(2.97 \times 10^{03})$	$(3.18 \times 10^{03})$	$(3.41 \times 10^{03})$	$(2.74 \times 10^{+03})$	$(2.85 \times 10^{+03})$	$(2.96 \times 10^{+03})$	$2.03 \times 10^{+03}$	$2.55 \times 10^{+03}$	$3.07 \times 10^{+03}$
3	$(1.57 \times 10^{04})$	$(1.68 \times 10^{04})$	$(1.80 \times 10^{04})$	$(1.41 \times 10^{+04})$	$(1.46 \times 10^{+04})$	$(1.52 \times 10^{+04})$	$1.01 \times 10^{+04}$	$1.28 \times 10^{+04}$	$1.55 \times 10^{+04}$
3.5	$(5.65 \times 10^{04})$	$(6.05 \times 10^{04})$	$(6.48 \times 10^{04})$	$(4.96 \times 10^{+04})$	$(5.16 \times 10^{+04})$	$(5.37 \times 10^{+04})$	$3.46 \times 10^{+04}$	$4.44 \times 10^{+04}$	$5.42 \times 10^{+04}$
4	$(1.56 \times 10^{05})$	$(1.67 \times 10^{05})$	$(1.79 \times 10^{05})$	$(1.36 \times 10^{+05})$	$(1.41 \times 10^{+05})$	$(1.47 \times 10^{+05})$	$9.40 \times 10^{+04}$	$1.22 \times 10^{+05}$	$1.50 \times 10^{+05}$
5	$(7.15 \times 10^{05})$	$(7.65 \times 10^{05})$	$(8.19 \times 10^{05})$	$(6.10 \times 10^{+05})$	$(6.34 \times 10^{+05})$	$(6.59 \times 10^{+05})$	$4.30 \times 10^{+05}$	$5.70 \times 10^{+05}$	$7.11 \times 10^{+05}$
6	$(2.11 \times 10^{06})$	$(2.26 \times 10^{06})$	$(2.42 \times 10^{06})$	$(1.80 \times 10^{+06})$	$(1.88 \times 10^{+06})$	$(1.95 \times 10^{+06})$	$1.28 \times 10^{+06}$	$1.74 \times 10^{+06}$	$2.20 \times 10^{+06}$
7	$(4.74 \times 10^{06})$	$(5.07 \times 10^{06})$	$(5.43 \times 10^{06})$	$(4.07 \times 10^{+06})$	$(4.23 \times 10^{+06})$	$(4.40 \times 10^{+06})$	$2.88 \times 10^{+06}$	$4.02 \times 10^{+06}$	$5.16 \times 10^{+06}$
8	$(8.85 \times 10^{06})$	$(9.47 \times 10^{06})$	$(1.01 \times 10^{07})$	$(7.70 \times 10^{+06})$	$(8.01 \times 10^{+06})$	$(8.32 \times 10^{+06})$	$5.37 \times 10^{+06}$	$7.69 \times 10^{+06}$	$1.00 \times 10^{+07}$
9	$(1.45 \times 10^{07})$	$(1.55 \times 10^{07})$	$(1.66 \times 10^{07})$	$(1.28 \times 10^{+07})$	$(1.33 \times 10^{+07})$	$(1.39 \times 10^{+07})$	$8.80 \times 10^{+06}$	$1.29 \times 10^{+07}$	$1.70 \times 10^{+07}$
10	$(2.13 \times 10^{07})$	$(2.28 \times 10^{07})$	$(2.44 \times 10^{07})$	$(1.97 \times 10^{+07})$	$(2.04 \times 10^{+07})$	$(2.12 \times 10^{+07})$	$1.29 \times 10^{+07}$	$1.96 \times 10^{+07}$	$2.63 \times 10^{+07}$

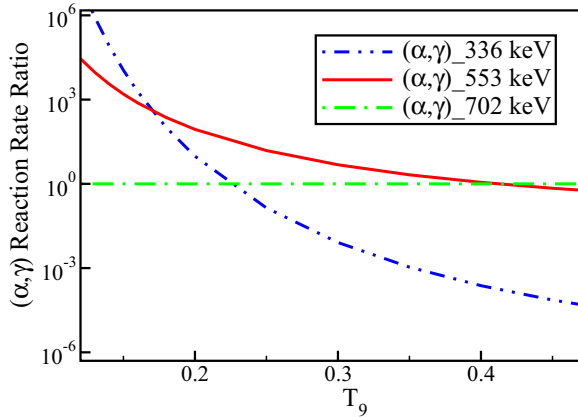


FIG. 8. Comparison between the reaction rates corresponding to individual resonances observed in the present work, above the  $\alpha$  threshold, normalized to the  $E_\alpha = 702$  keV resonance, which is the lowest directly observed resonance.

the efficiency of  $^{22}\text{Ne}$  neutron source more definitively. One of the future efforts being planned in this direction is the proposal to study  $^{22}\text{Ne}(\alpha, \gamma)^{26}\text{Mg}$  reaction in inverse kinematics using the 5U Accelerator, the helium jet gas target [94], and the St. George Recoil Separator [95] developed at the University of Notre Dame. The promising ability of the St. George Separator to effectively separate the beam from the reaction products will help reduce the beam-induced background, thereby allowing a better study of the  $^{22}\text{Ne} + \alpha$  low energy resonances in the direct reaction channel.

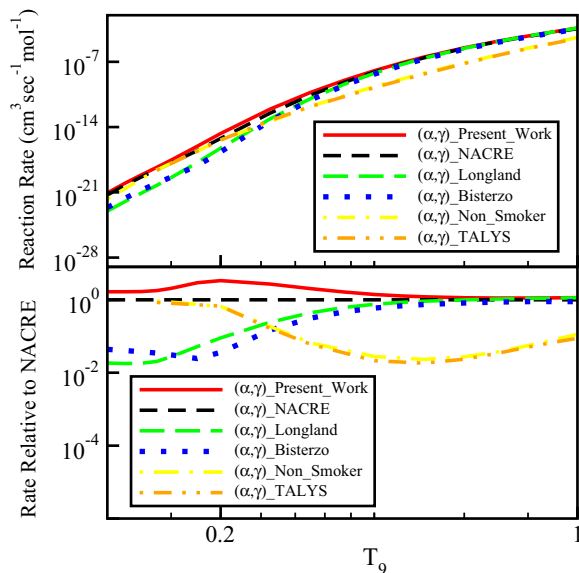


FIG. 9. The upper panel shows the comparison of the total  $^{22}\text{Ne}(\alpha, \gamma)^{26}\text{Mg}$  reaction rate calculated for the present work with the rates available in the literature. The lower panel shows the same comparison normalized to the NACRE total  $(\alpha, \gamma)$  rate [34].

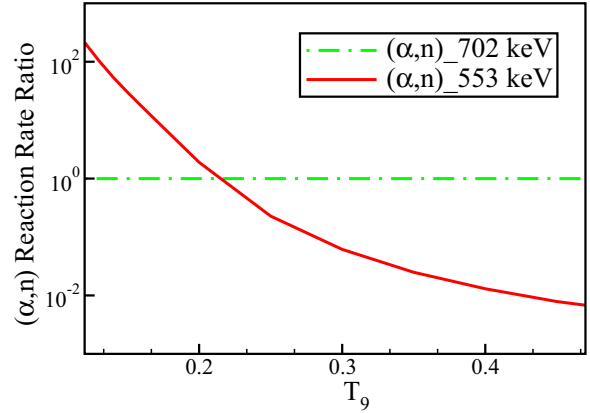


FIG. 10. Comparison between the reaction rates corresponding to individual resonances observed in the present work, above the  $n$  threshold, normalized to the  $E_\alpha = 702$  keV resonance, which is the lowest directly observed resonance.

### ACKNOWLEDGMENTS

We sincerely thank the RCNP staff for all their effort in delivering high quality  $\alpha$  and  $^6\text{Li}$  dispersion matched beams necessary for the present measurements. This work was funded by the National Science Foundation (NSF) through Grant No. PHY-1068192 and by the Joint Institute for Nuclear Astrophysics (JINA) through Grants No. PHY-0822648, No. PHY-09-22648, No. PHY-1430152, and No. PHY-0822648. Sara Bisterzo acknowledges support from the B2FH Association for the numerical calculations. Marco Pignatari acknowledges support via Grant No. EU MIRG-CT-2006-046520, from the “Lendület-2014” Program of the

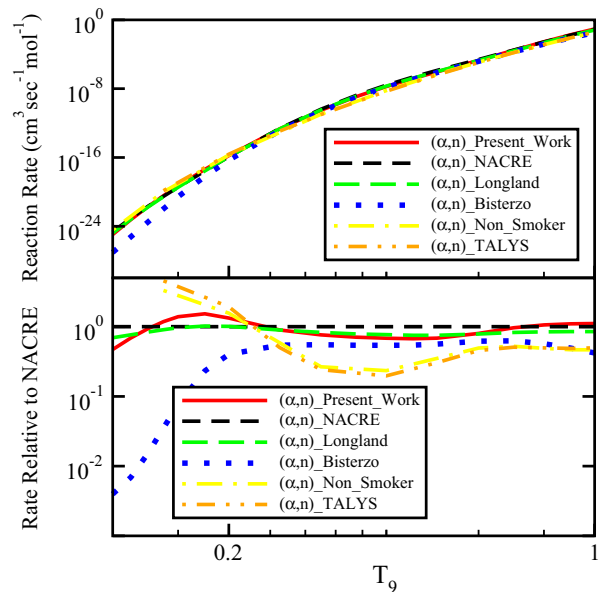


FIG. 11. The upper panel shows the comparison of the total  $^{22}\text{Ne}(\alpha, n)^{25}\text{Mg}$  reaction rate calculated for the present work with the rates available in the literature. The lower panel shows the same comparison normalized to the NACRE total  $(\alpha, n)$  rate [34].

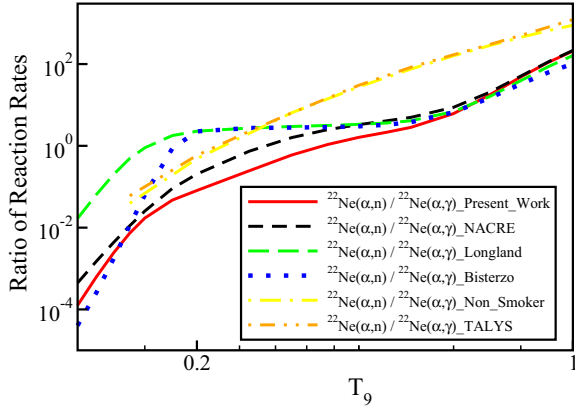


FIG. 12. Comparison of the  $^{22}\text{Ne}(\alpha, n)/^{22}\text{Ne}(\alpha, \gamma)$  reaction rate ratio for the present work with the literature rate ratios.

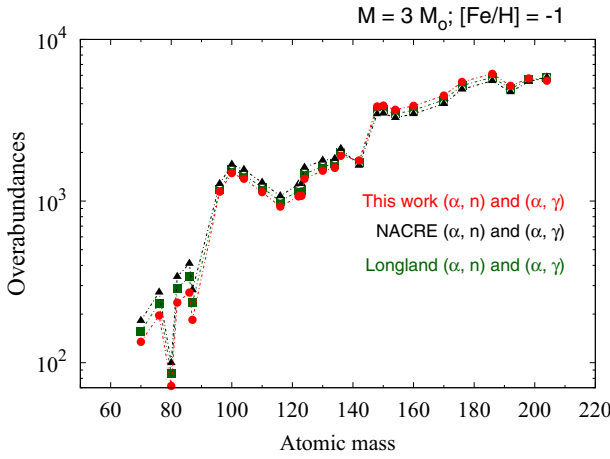


FIG. 13. Impact of  $^{22}\text{Ne} + \alpha$  capture rates on the isotopic overabundances for a  $3M_{\odot}$  AGB star at 1/10 solar metallicity. Comparison is shown between the impacts due to present  $\alpha$ -capture rates, Longland *et al.* rates [88], and NACRE rates [34].

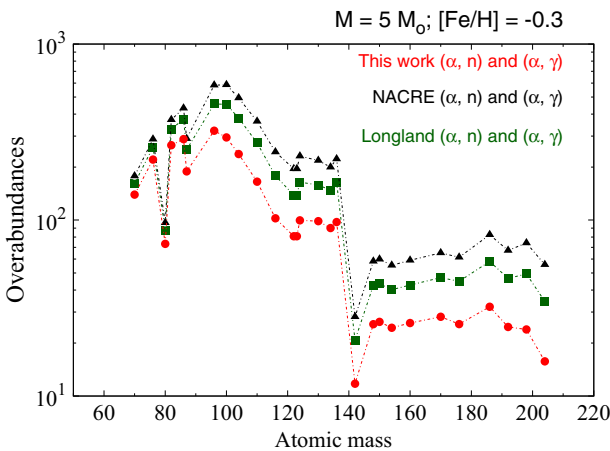


FIG. 14. Impact of  $^{22}\text{Ne} + \alpha$  capture rates on the isotopic overabundances for a  $5M_{\odot}$  AGB star at half solar metallicity. Comparison is shown between the impacts due to present  $\alpha$ -capture rates, Longland *et al.* rates [88], and NACRE rates [34].

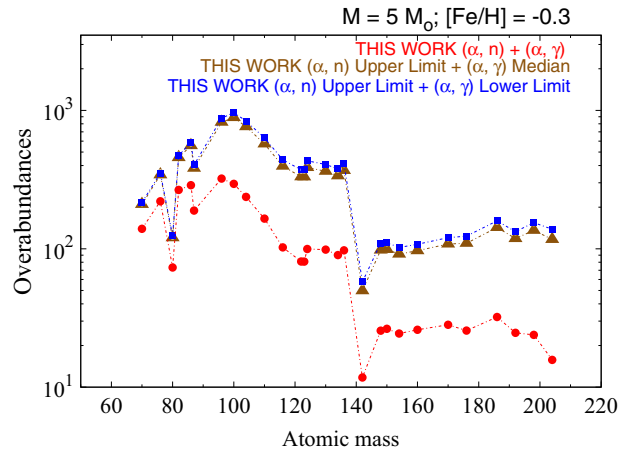


FIG. 15. Impact of present  $(\alpha, n)$  upper limit and  $(\alpha, \gamma)$  lower limit on the isotopic overabundances for a  $5M_{\odot}$  AGB star at half solar metallicity.

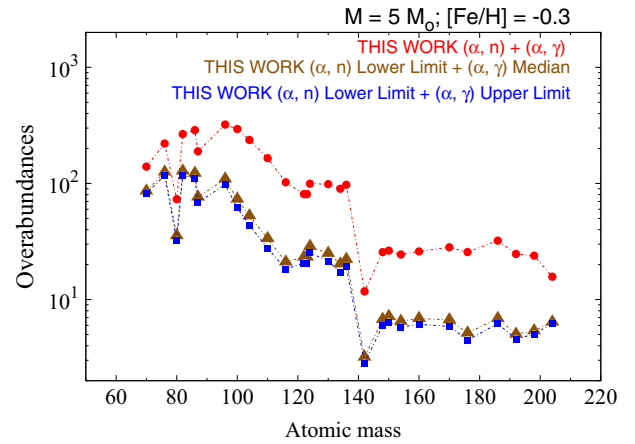


FIG. 16. Impact of present  $(\alpha, n)$  lower limit and  $(\alpha, \gamma)$  upper limit on the isotopic overabundances for a  $5M_{\odot}$  AGB star at half solar metallicity.

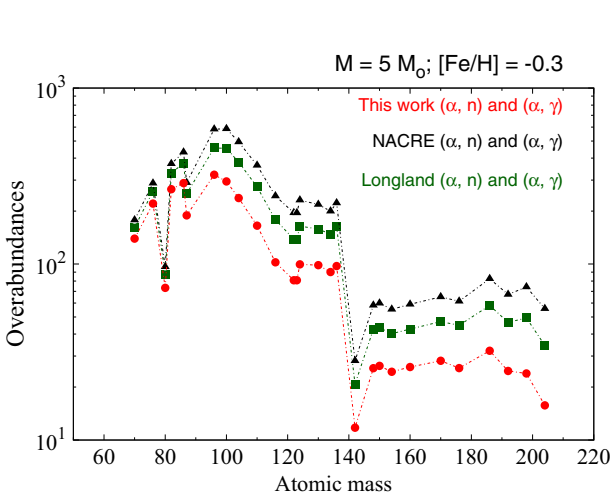


FIG. 17. Impact of  $^{22}\text{Ne} + \alpha$  capture rates on the  $s$ -process distribution for a  $25M_{\odot}$  massive star. Comparison is shown between the impacts due to the present  $\alpha$ -capture rates and a combination of Jaeger *et al.*  $^{22}\text{Ne}(\alpha, n)$  rates [54] and  $^{22}\text{Ne}(\alpha, \gamma)$  NACRE rates [34].

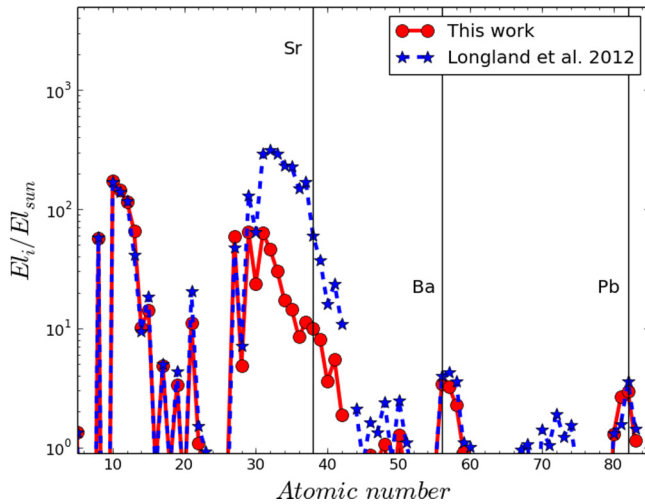


FIG. 18. Impact of  $^{22}\text{Ne} + \alpha$  capture rates on the  $s$ -process distribution for a  $25M_{\odot}$  massive star. Comparison is shown between the impacts due to present  $\alpha$ -capture rates and Longland *et al.* rates [88].

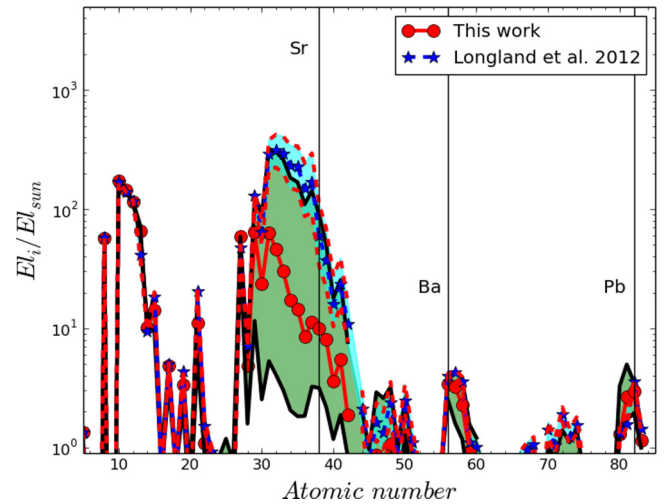


FIG. 19. Uncertainty range in the  $s$ -process distribution corresponding to Longland *et al.* [88] (light blue region) and present  $^{22}\text{Ne} + \alpha$  capture rates (green region).

Hungarian Academy of Sciences (Hungary), and from SNF (Switzerland). He also acknowledges PRACE, through its Distributed Extreme Computing Initiative, for resource allocations on Sisu (CSC, Finland), Archer (EPCC, UK), and Beskow (KTH, Sweden) and the support of STFC's DiRAC

High Performance Computing Facilities; DiRAC is part of the National E-infrastructure. Ongoing resource allocations on the University of Hulls High Performance Computing Facility, Viper, are gratefully acknowledged.

- [1] F. Käppeler, R. Gallino, S. Bisterzo, and W. Aoki, *Rev. Mod. Phys.* **83**, 157 (2011).
- [2] C. M. Raiteri, M. Busso, G. Picchio, and R. Gallino, *Astrophys. J.* **371**, 665 (1991).
- [3] R. Gallino, C. Arlandini, M. Busso, M. Lugaro, C. Travaglio, O. Straniero, A. Chieff, and M. Limongi, *Astrophys. J.* **497**, 338 (1998).
- [4] C. Sneden, J. J. Cowan, and R. Gallino, *Annu. Rev. Astron. Astrophys.* **46**, 241 (2008).
- [5] F.-K. Thielemann, A. Arcones, R. Käppeli, M. Liebendörfer, T. Rauscher, C. Winteler, C. Fröhlich, I. Dillmann, T. Fischer, G. Martinez-Pinedo *et al.*, in Particle and Nuclear Astrophysics: International Workshop on Nuclear Physics, 32nd Course [*Prog. Part. Nucl. Phys.* **66**, 346 (2011)].
- [6] F. van de Voort, E. Quataert, P. F. Hopkins, D. Kere, and C.-A. Faucher-Giguère, *Mon. Not. R. Astron. Soc.* **447**, 140 (2015).
- [7] B. Wehmeyer, M. Pignatari, and F.-K. Thielemann, *Mon. Not. R. Astron. Soc.* **452**, 1970 (2015).
- [8] G. Cescutti, D. Romano, F. Matteucci, C. Chiappini, and R. A. Hirschi, *Astron. Astrophys.* **577**, 139 (2015).
- [9] C. Arlandini, F. Käppeler, K. Wisshak, R. Gallino, M. Lugaro, M. Busso, and O. Straniero, *Astrophys. J.* **525**, 886 (1999).
- [10] S. Bisterzo, R. Gallino, O. Straniero, S. Cristallo, and F. Käppeler, *Mon. Not. R. Astron. Soc.* **418**, 284 (2011).
- [11] C. Travaglio, R. Gallino, E. Arnone, J. Cowan, F. Jordan, and C. Sneden, *Astrophys. J.* **601**, 864 (2004).
- [12] I. U. Roederer, J. J. Cowan, A. I. Karakas, K.-L. Kratz, M. Lugaro, J. Simmerer, K. Farouqi, and C. Sneden, *Astrophys. J.* **724**, 975 (2010).
- [13] S. Bisterzo, C. Travaglio, R. Gallino, M. Wiescher, and F. Käppeler, *Astrophys. J.* **787**, 10 (2014).
- [14] S. Bisterzo, R. Gallino, O. Straniero, S. Cristallo, and F. Käppeler, *Mon. Not. R. Astron. Soc.* **422**, 849 (2012).
- [15] M. Lugaro, C. L. Doherty, A. I. Karakas, S. T. Maddison, K. Liffman, D. A. García-Hernández, L. Siess, and J. C. Lattanzio, *Meteorit. Planet. Sci.* **47**, 1998 (2012).
- [16] T. Hansen, C. J. Hansen, N. Christlieb, D. Yong, T. C. Beers, and J. Andersen, *arXiv:1503.01990*.
- [17] K. De Smedt, H. Van Winckel, A. I. Karakas, L. Siess, S. Goriely, and P. R. Wood, *Astron. Astrophys.* **541**, A67 (2012).
- [18] K. De Smedt, H. Van Winckel, D. Kamath, A. I. Karakas, L. Siess, S. Goriely, and P. R. Wood, *Astron. Astrophys.* **563**, L5 (2014).
- [19] M. Busso, R. Gallino, D. L. Lambert, C. Travaglio, and V. V. Smith, *Astrophys. J.* **557**, 802 (2001).
- [20] M. Busso, R. Gallino, and G. J. Wasserburg, *Annu. Rev. Astron. Astrophys.* **37**, 239 (1999).
- [21] A. I. Karakas and J. C. Lattanzio, *Pub. Astron. Soc. Aust.* **31**, e030 (2014).
- [22] S. V. Eck, S. Goriely, A. Jorissen, and B. Plez, *Astron. Astrophys.* **404**, 291 (2003).
- [23] M. Pignatari, R. Gallino, G. Meynet, R. Hirschi, F. Herwig, and M. Wiescher, *Astrophys. J. Lett.* **687**, L95 (2008).
- [24] G. Cescutti, C. Chiappini, R. Hirschi, G. Meynet, and U. Frischknecht, *Astron. Astrophys.* **553**, A51 (2013).
- [25] U. Frischknecht, R. Hirschi, and F.-K. Thielemann, *Astron. Astrophys.* **538**, L2 (2012).

- [26] B. Sharpee, Y. Zhang, R. Williams, E. Pellegrini, K. Cavagnolo, J. A. Baldwin, M. Phillips, and X.-W. Liu, *Astrophys. J.* **659**, 1265 (2007).
- [27] E. Zinner, *Annu. Rev. Earth Planet. Sci.* **26**, 147 (1998).
- [28] L.-S. The, M. F. E. Eid, and B. S. Meyer, *Astrophys. J.* **655**, 1058 (2007).
- [29] M. Pignatari, R. Gallino, M. Heil, M. Wiescher, F. Käppeler, F. Herwig, and S. Bisterzo, *Astrophys. J.* **710**, 1557 (2010).
- [30] O. Straniero, S. Cristallo, and L. Piersanti, *Astrophys. J.* **785**, 77 (2014).
- [31] N. Prantzos, M. Hashimoto, and K. Nomoto, *Astron. Astrophys.* **234**, 211 (1990).
- [32] W. D. Arnett and J. W. Truran, *Astrophys. J.* **157**, 339 (1969).
- [33] N. Liu, M. R. Savina, A. M. Davis, R. Gallino, O. Straniero, F. Gyngard, M. J. Pellin, D. G. Willingham, N. Dauphas, M. Pignatari *et al.*, *Astrophys. J.* **786**, 66 (2014).
- [34] C. Angulo, M. Arnould, M. Rayet, P. Descouvemont, D. Baye, C. Leclercq-Willain, A. Coc, S. Barhoumi, P. Aguer, C. Rolfs *et al.*, *Nucl. Phys. A* **656**, 3 (1999).
- [35] F. Käppeler, M. Wiescher, U. Giesen, J. Görres, I. Baraffe, M. El Eid, C. M. Raiteri, M. Busso, R. Gallino, M. Limongi *et al.*, *Astrophys. J.* **437**, 396 (1994).
- [36] A. Aprahamian, K. Langanke, and M. Wiescher, *Prog. Part. Nucl. Phys.* **54**, 535 (2005).
- [37] K. Ikeda, N. Takigawa, and H. Horiuchi, *Prog. Theor. Phys. Suppl.* **68**, 464 (1968).
- [38] M. Freer, *Rep. Prog. Phys.* **70**, 2149 (2007).
- [39] A. Volya and Y. M. Tchuvil'sky, *Phys. Rev. C* **91**, 044319 (2015).
- [40] P. E. Hodgson, *Nuclear Reactions and Nuclear Structure* (Clarendon Press, Oxford, 1971).
- [41] *Clusters in Nuclei Vol. 1*, edited by C. Beck, Lecture Notes in Physics Vol. 818 (Springer-Verlag, Berlin, 2010).
- [42] *Clusters in Nuclei Vol. 2*, edited by C. Beck, Lecture Notes in Physics Vol. 848 (Springer-Verlag, Berlin, 2012).
- [43] *Clusters in Nuclei Vol. 3*, edited by C. Beck, Lecture Notes in Physics Vol. 875 (Springer-Verlag, Berlin, 2015).
- [44] E. Epelbaum, H. Krebs, D. Lee, and Ulf-G. Meißner, *Phys. Rev. Lett.* **106**, 192501 (2011).
- [45] C. R. Brune, W. H. Geist, R. W. Kavanagh, and K. D. Veal, *Phys. Rev. Lett.* **83**, 4025 (1999).
- [46] S. Dababneh, M. Heil, F. Käppeler, J. Görres, M. Wiescher, R. Reifarth, and H. Leiste, *Phys. Rev. C* **68**, 025801 (2003).
- [47] E. Johnson, G. Rogachev, V. Goldberg, S. Brown, D. Robson, A. Crisp, P. Cottle, C. Fu, J. Giles, B. Green *et al.*, *Eur. Phys. J. A* **42**, 135 (2009).
- [48] U. Giesen, C. Browne, J. Görres, S. Graff, C. Iliadis, H.-P. Trautvetter, M. Wiescher, W. Harms, K. Kratz, B. Pfeiffer *et al.*, *Nucl. Phys. A* **561**, 95 (1993).
- [49] D. Ashery, *Nucl. Phys. A* **136**, 481 (1969).
- [50] F. X. Haas and J. K. Bair, *Phys. Rev. C* **7**, 2432 (1973).
- [51] H. Drotleff, A. Denker, J. Hammer, H. Knee, S. Küchler, D. Streit, C. Rolfs, and H. Trautvetter, *Z. Phys. A* **338**, 367 (1991).
- [52] V. Harms, K.-L. Kratz, and M. Wiescher, *Phys. Rev. C* **43**, 2849 (1991).
- [53] K. Wolke, V. Harms, H. Becker, J. Hammer, K. Kratz, C. Rolfs, U. Schröder, H. Trautvetter, M. Wiescher, and A. Wöhr, *Z. Phys. A* **334**, 491 (1989).
- [54] M. Jaeger, R. Kunz, A. Mayer, J. W. Hammer, G. Staudt, K. L. Kratz, and B. Pfeiffer, *Phys. Rev. Lett.* **87**, 202501 (2001).
- [55] E. Kuhlmann, E. Ventura, J. R. Calarco, D. G. Mavis, and S. S. Hanna, *Phys. Rev. C* **11**, 1525 (1975).
- [56] C. Moss, *Nucl. Phys. A* **269**, 429 (1976).
- [57] G. M. Crawley, C. Djalali, N. Marty, M. Morlet, A. Willis, N. Anantaraman, B. A. Brown, and A. Galonsky, *Phys. Rev. C* **39**, 311 (1989).
- [58] K. V. D. Borg, M. Harakeh, and A. V. D. Woude, *Nucl. Phys. A* **365**, 243 (1981).
- [59] C. Ugalde, A. E. Champagne, S. Daigle, C. Iliadis, R. Longland, J. R. Newton, E. Osenbaugh-Stewart, J. A. Clark, C. Deibel, A. Parikh *et al.*, *Phys. Rev. C* **76**, 025802 (2007).
- [60] C. Massimi, P. Koehler, S. Bisterzo, N. Colonna, R. Gallino, F. Gunsing, F. Käppeler, G. Lorusso, A. Mengoni, M. Pignatari *et al.*, *Phys. Rev. C* **85**, 044615 (2012).
- [61] R. Longland, C. Iliadis, G. Rusev, A. P. Tonchev, R. J. deBoer, J. Görres, and M. Wiescher, *Phys. Rev. C* **80**, 055803 (2009).
- [62] G. Audi and A. Wapstra, *Nucl. Phys. A* **595**, 409 (1995).
- [63] H. Weigmann, R. L. Macklin, and J. A. Harvey, *Phys. Rev. C* **14**, 1328 (1976).
- [64] Y. Fujita (private communication).
- [65] R. J. deBoer, M. Wiescher, J. Görres, R. Longland, C. Iliadis, G. Rusev, and A. P. Tonchev, *Phys. Rev. C* **82**, 025802 (2010).
- [66] R. J. deBoer, A. Best, J. Görres, K. Smith, W. Tan, M. Wiescher, R. Raut, G. Rusev, A. P. Tonchev, and W. Tornow, *Phys. Rev. C* **89**, 055802 (2014).
- [67] W. A. Fowler, C. C. Lauritsen, and T. Lauritsen, *Rev. Mod. Phys.* **20**, 236 (1948).
- [68] J. J. Kraushaar, M. Fujiwara, K. Hosono, H. Ito, M. Kondo, H. Sakai, M. Tosaki, M. Yasue, S. I. Hayakawa, and R. J. Peterson, *Phys. Rev. C* **34**, 1530 (1986).
- [69] T. Wakasa, K. Hatanaka, Y. Fujita, G. Berg, H. Fujimura, H. Fujita, M. Itoh, J. Kamiya, T. Kawabata, K. Nagayama *et al.*, *Nucl. Instrum. Methods Phys. Res. Sect. A* **482**, 79 (2002).
- [70] Y. Fujita, K. Hatanaka, G. Berg, K. Hosono, N. Matsuoka, S. Morinobu, T. Noro, M. Sato, K. Tamura, and H. Ueno, *Nucl. Instrum. Methods Phys. Res. Sect. B* **126**, 274 (1997).
- [71] H. Fujita, Y. Fujita, G. Berg, A. Bacher, C. Foster, K. Hara, K. Hatanaka, T. Kawabata, T. Noro, H. Sakaguchi *et al.*, *Nucl. Instrum. Methods Phys. Res. Sect. A* **484**, 17 (2002).
- [72] M. Fujiwara, H. Akimune, I. Daito, H. Fujimura, Y. Fujita, K. Hatanaka, H. Ikegami, I. Katayama, K. Nagayama, N. Matsuoka *et al.*, *Nucl. Instrum. Methods Phys. Res. Sect. A* **422**, 484 (1999).
- [73] H. Fujita, G. Berg, Y. Fujita, K. Hatanaka, T. Noro, E. Stephenson, C. Foster, H. Sakaguchi, M. Itoh, T. Taki *et al.*, *Nucl. Instrum. Methods Phys. Res. Sect. A* **469**, 55 (2001).
- [74] H. Matsubara, A. Tamii, Y. Shimizu, K. Suda, Y. Tameshige, and J. Zenihiro, *Nucl. Instrum. Methods Phys. Res. Sect. A* **678**, 122 (2012).
- [75] T. Tanabe, M. Yasue, K. Sato, K. Ogino, Y. Kadota, Y. Taniguchi, K. Obori, K. Makino, and M. Tochi, *Phys. Rev. C* **24**, 2556 (1981).
- [76] N. Anantaraman, H. Gove, J. Töke, and J. Draayer, *Nucl. Phys. A* **279**, 474 (1977).
- [77] P. Endt, *Nucl. Phys. A* **633**, 1 (1998).
- [78] D. Tilley, C. Cheves, J. Kelley, S. Raman, and H. Weller, *Nucl. Phys. A* **636**, 249 (1998).
- [79] R. Firestone, *Nucl. Data Sheets* **108**, 2319 (2007).
- [80] J. F. Ziegler, <http://www.srim.org/>
- [81] M. H. Macfarlane and S. C. Pieper, <http://www.phy.anl.gov/theory/ptolemy>
- [82] I. J. Thompson, <http://www.fresco.org.uk>
- [83] J. Cook, *Nucl. Phys. A* **388**, 153 (1982).

- [84] H. An and C. Cai, *Phys. Rev. C* **73**, 054605 (2006).
- [85] P. E. Koehler, *Phys. Rev. C* **66**, 055805 (2002).
- [86] J. Hammer, B. Fischer, H. Hollick, H. Trautvetter, K. Kettner, C. Rolfs, and M. Wiescher, *Nucl. Instrum. Methods* **161**, 189 (1979).
- [87] M. Jaeger, Ph.D. thesis, University of Stuttgart, 2001 (unpublished), <http://elib.uni-stuttgart.de/opus/volltexte/2002/1066/>
- [88] R. Longland, C. Iliadis, and A. I. Karakas, *Phys. Rev. C* **85**, 065809 (2012).
- [89] F. Milder, J. Jänecke, and F. Becchetti, *Nucl. Phys. A* **276**, 72 (1977).
- [90] A. L. Sallaska, C. Iliadis, A. E. Champagne, S. Goriely, S. Starrfield, and F. X. Timmes, *Astrophys. J. Suppl. Ser.* **207**, 18 (2013).
- [91] R. H. Cyburt, A. M. Amthor, R. Ferguson, Z. Meisel, K. Smith, S. Warren, A. Heger, R. D. Hoffman, T. Rauscher, A. Sakharuk *et al.*, *Astrophys. J. Suppl. Ser.* **189**, 240 (2010).
- [92] S. Bisterzo, R. Gallino, F. Käppeler, M. Wiescher, G. Imbriani, O. Straniero, S. Cristallo, J. Görres, and R. J. deBoer, *Mon. Not. R. Astron. Soc.* **449**, 506 (2015).
- [93] S. Goriely, S. Hilaire, and A. J. Koning, *Astron. Astrophys.* **487**, 767 (2008).
- [94] A. Kontos, D. Schürmann, C. Akers, M. Couder, J. Görres, D. Robertson, E. Stech, R. Talwar, and M. Wiescher, *Nucl. Instrum. Methods Phys. Res. Sect. A* **664**, 272 (2012).
- [95] M. Couder, G. Berg, J. Görres, P. LeBlanc, L. Lamm, E. Stech, M. Wiescher, and J. Hinnefeld, *Nucl. Instrum. Methods Phys. Res. Sect. A* **587**, 35 (2008).